USAFA-TN-84-9

AD-A149 799

Department of Aeronautics
Dean of the Faculty
United States Air Force Academy
Colorado Springs
Colorado 80840-5831

THE SEVEN-HOLE PRESSURE PROBE

TECHNICAL NOTE
USAFA-TN-84-9

Reed,L.
Mattingly,J.D.
Jonas,F.M.
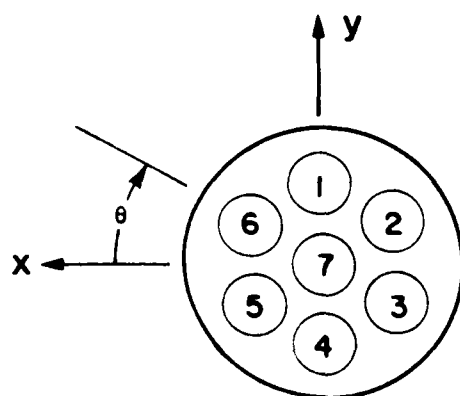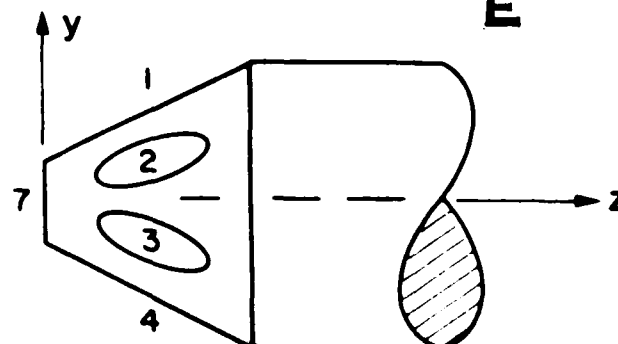
DTIC FILE COPY

DTIC
S ELECTE D
JAN 2 5 1985
E

FRONT VIEW   SIDE VIEW

85 01 15 129
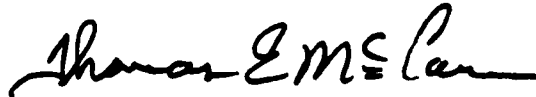
Any views expressed in this paper are those of the authors. They should not be interpreted as reflecting the views of the USAF Academy or the official opinion of any governmental agency. Notes are not reviewed for content or quality by the USAF Academy but are published primarily as a service to the faculty to facilitate internal research communication.

This Technical Note has been cleared for open publication and/or public release by the appropriate Office of Information in accordance with AFR 190-1 and DODD 5230.9. There is no objection to unlimited distribution of this Technical Note to the public at large or by DDC to the National Technical Information Service.

This Technical Note is approved for publication.

THOMAS E. McCANN, Lt Colonel, USAF
Director of Research and Computer Based Education

Forward

This technical note is the final report covering the period 1 Oct 83 to 30 Sep 84 in response to NASA A 10498C sponsored by the NASA Ames Research Center and administerd by Mr. W.P. Nelms, and in response to AMD/RDS 84-16 sponsored by AFAMRL/CC (CREST) and administered by Major A.M. Higgins. Majors Frederick M. Jonas and Jack D. Mattingly were the principal investigators for this effort, aided by the faculty and cadets at the Air Force Academy. Of particular note is the contribution of 2Lt Lawrence Reed, former student and now Air Force officer, who is the principal author for this paper. The paper documents the current status of the seven-hole probe developed at the Air Force Academy under the sponsorship of the NASA Ames Research Center.

Accession For	
NTIS GRA&I	☒
DTIC TAB	☐
Unannounced	☐
Justification	
By	
Distribution/	
Availability Codes	
	Avail and/or
Dist	Special
A-1	

DTIC
COPY
INSPECTED

THE SEVEN-HOLE PRESSURE PROBE

Lawrence Reed*, Jack D. Mattingly**, and Frederick Jonas**

Abstract

This paper documents recent and past developments with respect to the seven-hole pressure probe. Included are discussions on probe design, construction, calibration, and measurement capabilities. The effects on probe measurements in shear flows, as well as methods of correction, are also included. Finally, research applications in the measurement of unknown flowfields are presented. As shown, the seven-hole pressure probe is a valuable and highly accurate device for qualitatively or quantitatively documenting unknown flowfields.

I. Introduction

The purpose of this paper is to document recent and past developments with respect to the seven-hole pressure probe developed at the United States Air Force Academy in conjunction with the NASA Ames Research Center. As with all pressure probes, the seven-hole probe can be used to map unknown internal or external flowfields, giving valuable information to the aerodynamicist. The advantage of the seven-hole probe over other flowfield measuring devices is its widely expanded measurement range and flexibility. To document this effort, Section II presents brief background material about the probe's design and use. Section III includes an overview of probe calibration in uniform flows, both compressible and incompressible. In Section IV, recent results of investigations into probe measurement capabilities in shear flow environments are presented. Measurement capabilities as well as measurement sources of error

*2nd Lt., USAF, Graduate Student, Univ. of Washington

**Major, USAF, Associate Professor, Dept. of Aeronautics

are discussed in Section V. Finally, recent research efforts on
the application of seven hole probe measurements in unknown flows
are presented in Section VI.

II. Background

Numerous techniques are available to measure unknown flow
fields. While methods such as tufts, streamers, and vanes are
primarily used for flow visualization, they are insufficient for
quantitative information. Detailed data on flow size, direction,
and pressure usually require direct obtrusive flow measurement.

One of the oldest known quantitative techniques may be found
in the pressure probe. Although other techniques, such as hot wire
anemometers and laser doppler anemometers, have been developed,
pressure probes are desirable from a flight vehicle standpoint
because of their simplicity and ruggedness (Ref 1). Coupled with
relatively low cost, pressure probes are an excellent measurement
device for research, development, and industrial applications.

One of the classic problems in obtrusive flow measurement is
the disturbance caused by a probe to the flow field it is
measuring. For certain applications, such as aircraft pitot-static
tubes, this sort of flow perturbation is relatively unimportant.

low distances for other applications

was developed at the United States Air Force Academy to increase the measurement range of a non-nulling pressure probe while minimizing probe size.

A.   Nulling Versus Stationary Probes

The increased measurement range of a multi-hole probe revolves on its ability to sense more pressures at the face of the probe. Two procedures, nulling and stationary, may be used to acquire the pressure data. A nulling probe is rotated in one or two planes until opposing peripheral ports measure equal pressures. The corresponding angle of rotation determines the flow angle. For the non-nulling approach, the probe is held stationary as pressures in opposing peripheral ports are recorded. The pressure differences are then transformed to flow angles through previously known calibration relationships. Although the nulling procedure allows analysis of high angle flow, it is mechanically complex, time consuming, and hence, may not be cost effective. On the other hand, stationary probes with up to five holes are incapable of accurate measurements at high local flow angles (greater than 30 degrees) because of flow separation around the probe tip. Explained in detail in a later section, the seven hole probe is the only non-nulling probe that can determine flow angles up to 70 degrees relative to its axis. When combined with a computerized data acquisition system, the probe may record nearly two data points per second. This rate is significantly faster than current nulling devices, which require considerable time for the balancing of probe tip pressures before each measurement can be taken (Ref. 2).

B.   Analytical Model of Pressure Probe

Pressure probes used for measurement of flow direction and magnitude normally consist of an aerodynamic body with a symmetrical arrangement of sensing holes (Figure 1). Some typical geometries for pressure probes are reviewed in References 3 through 17 and pressure probes are treated in more general terms in References 18 and 19.
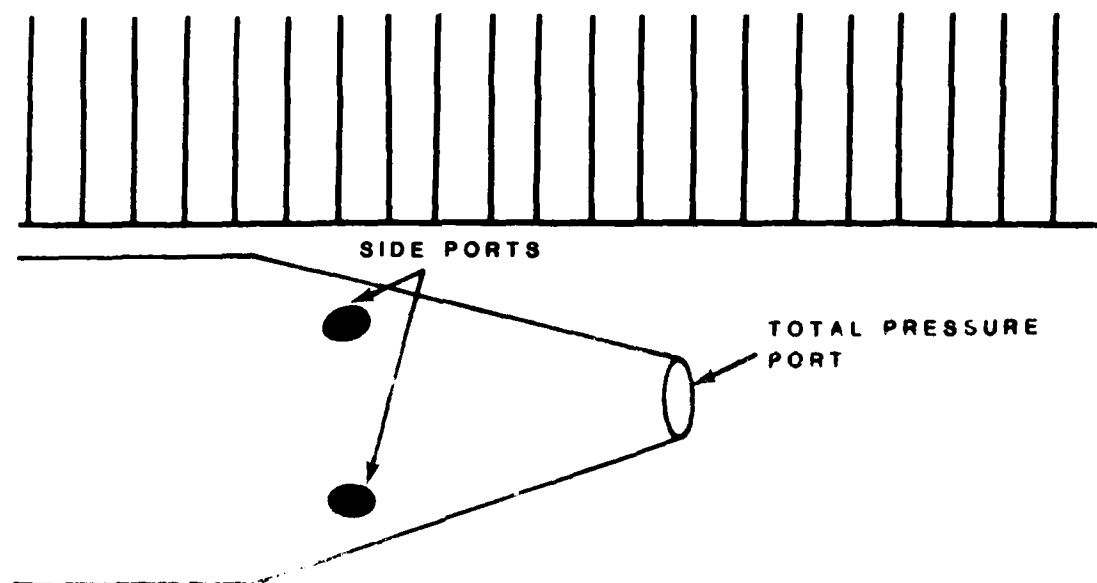

Figure 1. TYPICAL FLOW DIRECTION PROBE
(EACH UNIT ON SCALE REPRESENTS 0.65 in)

When the pressure probes of interest are to be used without flow, the sensitivity to flow angularity is extremely [...]

While numerically solving the three-dimensional potential flow
equations for the flow around an aerodynamic probe may be more
accurate than slender body theory under some conditions (Ref. 21
and 22), it does not lend itself to synthesis of probe shapes. The
slender body approach to the analysis of the probe provides a basis
for formulating analytic calibration relations and considerable
insight into the physical process.
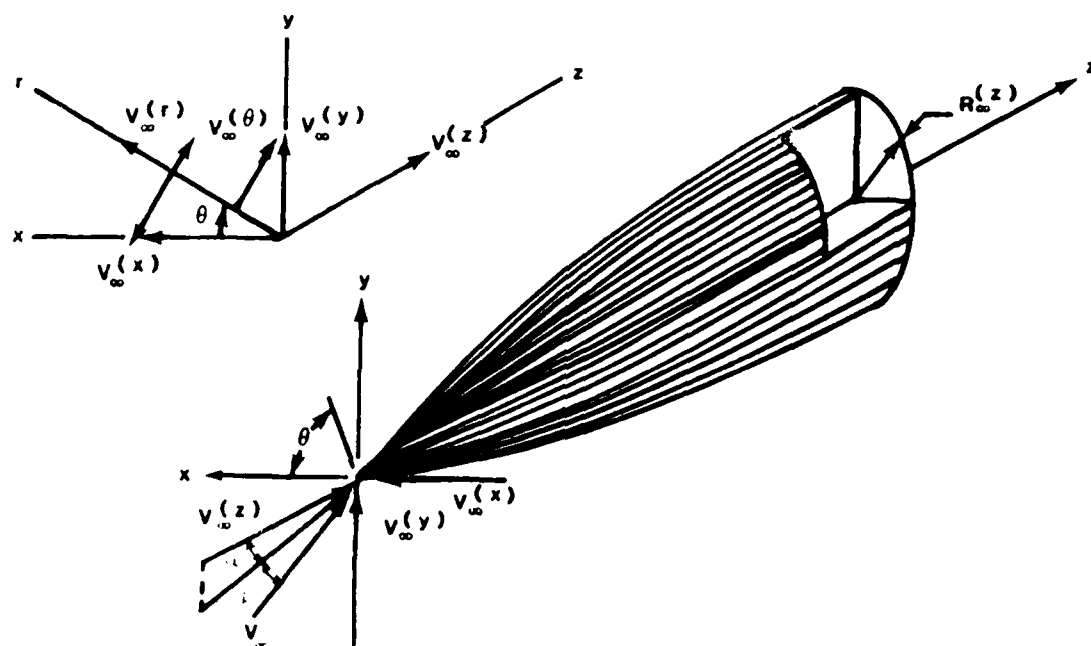
Figure 2. SLENDER BODY OF REVOLUTION IN A CROSS-FLOW (REF.18)

Huffman modeled the probe as a yawed body of revolution as
shown in Figure 2. For a slender body, the equation of motion is
linear and Huffman wrote the velocity potential as the sum of the
axial flow and the cross flow components (this follows a method
specified by Liepmann and Roshko, Ref. 23). Solution of the
equation of motion yielded the following velocity field in
cylindrical coordinates:

6

$$\frac{v_r}{V_\infty} = R'\frac{R}{r}(\cos\alpha\,\cos\beta) + (1-\frac{R^2}{r^2})(\sin\beta\,\cos\theta + \sin\alpha\,\cos\beta\,\sin\theta)$$

$$\frac{v_\theta}{V_\infty} = (1 + \frac{R^2}{r^2})(\sin\alpha\,\cos\beta\,\cos\theta - \sin\beta\,\sin\theta) \tag{1}$$

$$\frac{v_z}{V_\infty} = (1+\frac{f}{2})(\cos\alpha\,\cos\beta) + 2R'\frac{R}{r}(\sin\beta\,\cos\theta + \sin\alpha\,\cos\beta\,\sin\theta)$$

where f denotes the body-geometry function given by

$$f = -\frac{1}{2}(R^2)'\left(\frac{1}{\sqrt{z^2+\delta^2 r^2}} - \frac{1}{\sqrt{(\ell-z)^2+\delta^2 r^2}}\right)$$

$$+\frac{1}{2}(R^2)''\left[\frac{\ell-z}{\sqrt{(\ell-z)^2+\delta^2 r^2}} + \frac{z}{\sqrt{z^2+\delta^2 r^2}} + \ell n\left(\frac{-z+\sqrt{z^2+\delta^2 r^2}}{\ell-z+\sqrt{(\ell-z)^2+\delta^2 r^2}}\right)\right] \tag{2}$$

$$-\frac{1}{4}(R^2)'''\left(\frac{z^2}{\sqrt{z^2+\delta^2 r^2}} - \frac{(\ell-z)^2}{\sqrt{(\ell-z)^2+\delta^2 r^2}}+2\sqrt{(\ell-z)^2+\delta^2 r^2}-2\sqrt{z^2+\delta^2 r^2}\right) + \dots$$

The superscript prime (') denotes the derivative with respect to the variable z, and $\delta = 1-M_\infty^2$.

The pressure coefficient is defined as

$$C_p = \frac{P-P_\infty}{\frac{1}{2}\rho V_\infty^2} = 1-\frac{V^2}{V_\infty^2} \tag{3}$$

And when evaluated on the body the following expression results:

$$C_p = \dots \cos\ \ \cos^2\beta + \sin^2\beta\ [1-4\sin^2\ \ -4(R')\ \ \cos^2\ ] \tag{4}$$

$$\dots (R')\ \ \sin^2\ [2-\sin\alpha\,\sin\beta\,\sin^2\ (1-4R')\ \dots$$

$$\dots \cos^2 - \delta^2 \dots$$

where f is to be evaluated on the body surface, i.e. r=R, Equation
4 represents the major result of Huffman's analysis and can be used
to determine probe angular and static pressure sensitivity for
arbitrary geometries.

The pressure difference between ports on opposite sides of the
probe is used to determine the flow angularity. Since the side
ports of the probe are at the same z and r locations, the pressure
difference is proportional to the difference of C_p values at
different Θ locations and

$$
\begin{aligned}
P_i - P_j = 4\sin^2\alpha\ [\sin^2\Theta_j - \sin^2\Theta_i + (R')^2(\cos^2\Theta_j - \cos^2\Theta_i)] \\
+ 4\sin^2\alpha\cos^2\beta\ [\cos^2\Theta_j - \cos^2\Theta_i + (R')^2(\sin^2\Theta_j - \sin^2\Theta_i)] \\
+ 2\sin\alpha\sin2\beta\ [1-(R')^2]\ [\sin2\Theta_i - \sin2\Theta_j] \\
- 2R'(1+f/2)[\cos\alpha\sin2\beta\ (\cos\Theta_i - \cos\Theta_j) + \sin2\alpha\cos^2\beta(\sin\Theta_i - \sin\Theta_j)]
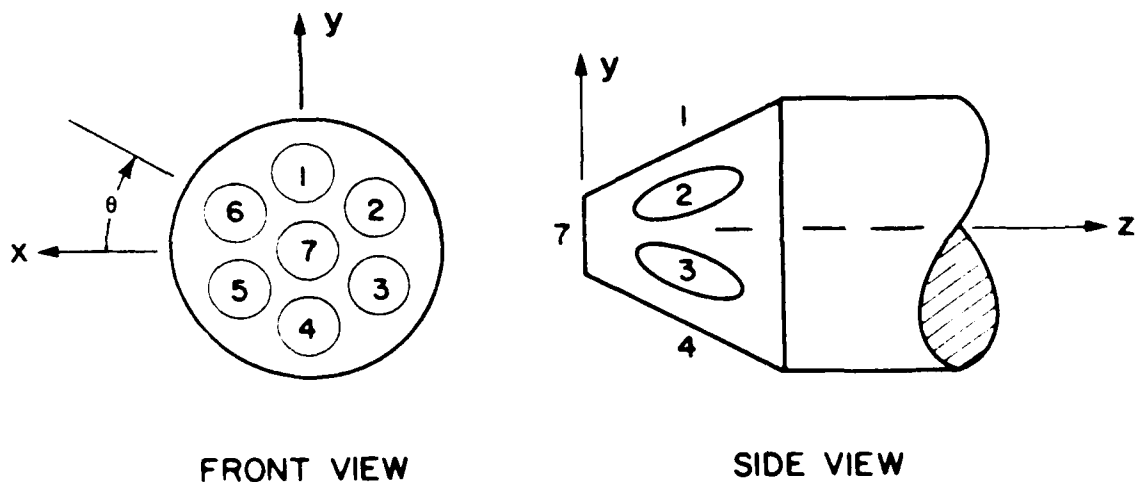\end{aligned}
\tag{5}
$$

FRONT VIEW   SIDE VIEW

Figure 3. SEVEN-HOLE PROBE

For the seven-hole probe shown in Figure 3, the six holes on the side face are located at $\theta_1 = 90°$, $\theta_2 = 150°$, $\theta_3 = 210°$, $\theta_4 = 270°$, $\theta_5 = 330°$, and $\theta_6 = 30°$. The resulting three pressure coefficient differences for opposite side holes are

$$\Delta C_1 = C_{p_4} - C_{p_1} = 4R'(1+f/2) \sin 2\alpha \cos^2\beta$$

$$\Delta C_2 = C_{p_3} - C_{p_6} = 2R'(1+f/2)[3\cos\alpha \sin 2\beta + \sin 2\alpha \cos^2\beta]$$

$$\Delta C_3 = C_{p_2} - C_{p_5} = 2R'(1+f/2)[3\cos\alpha \sin 2\beta - \sin 2\alpha \cos^2\beta]$$

(6)

These three pressure coefficients can be combined into a coefficient that is mainly dependent on the flow angle α and another coefficient that is mainly dependent on the flow angle β as follows:

$$\Delta C_\alpha = \frac{2\Delta C_1 + \Delta C_2 - \Delta C_3}{3} = 4R'(1+f/2) \sin 2\alpha \cos^2\beta$$

$$\Delta C_\beta = \frac{\Delta C_2 + \Delta C_3}{\sqrt{3}} = 4R'(1+f/2) \cos\alpha \sin 2\beta$$

(7)

The sensitivity to changes in flow angle is defined as $\frac{\partial \Delta C_\alpha}{\partial \alpha}$ or $\frac{\partial \Delta C_\beta}{\partial \beta}$. These sensitivities are

$$\frac{\partial \Delta C_\alpha}{\partial \alpha} = 8R'(1+f/2) \cos 2\alpha \cos^2\beta$$

$$\frac{\partial \Delta C_\beta}{\partial \beta} = 8R'(1+f/2) \cos\alpha \cos 2\beta$$

Also, the sensitivity is proportional to the slope of the probe's surface, R'. Equation 8 is plotted in Figure 4 for f=0. It is quite apparent from the figure that the probe angularity sensitivity -- regardless of shape -- depends on α and β. Approximately a 10% reduction in sensitivity occurs for α and β values of 10°. Note that $\partial\Delta C\alpha/\partial\alpha$ is the same for both positive and negative values of α and β.
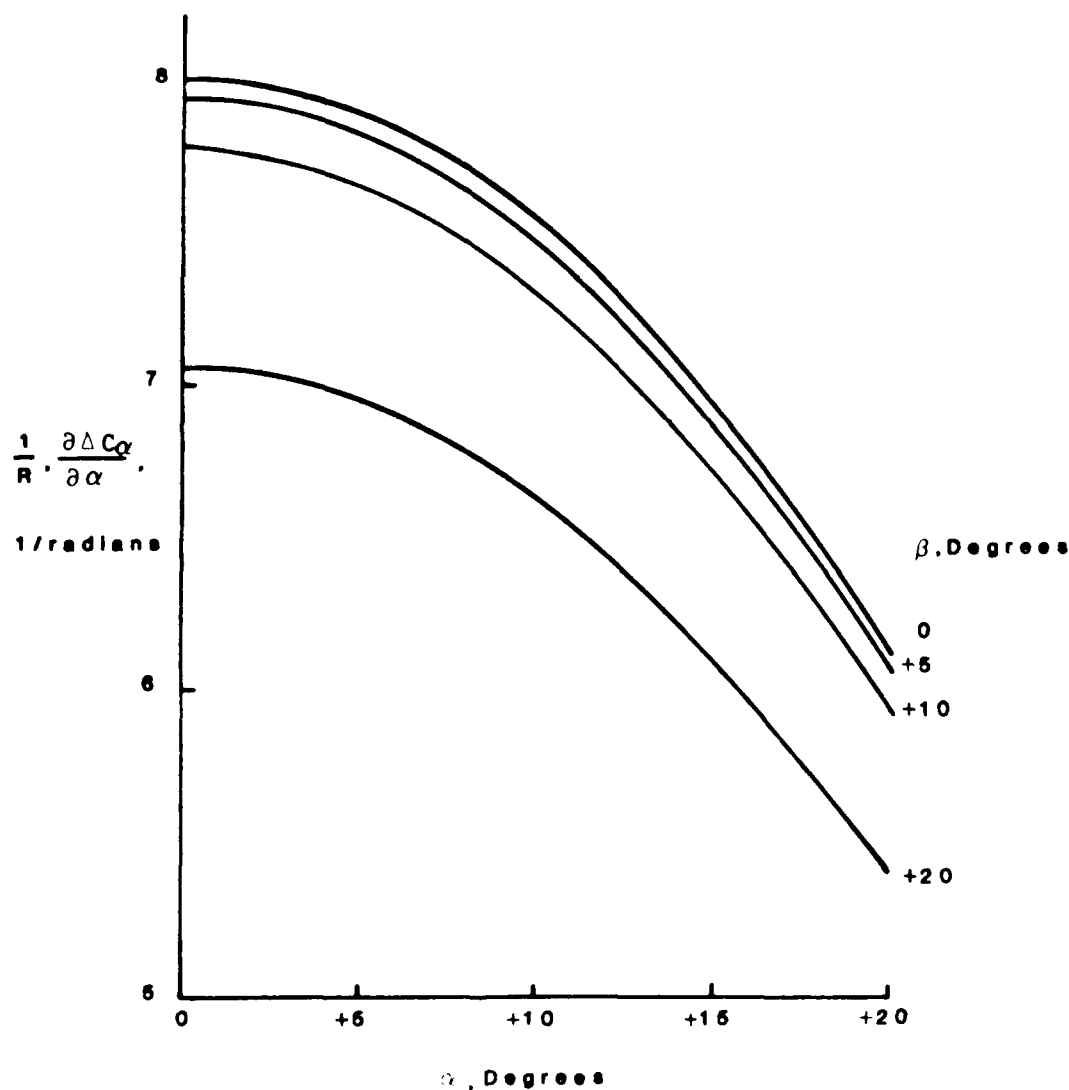

Figure 4. PROBE ANGULAR SENSITIVITY AS
A FUNCTION OF α AND β (REF. 18)

The average pressure coefficient can be used to determine the flow-field static pressure, P_∞. C_p is evaluated at a number of theta values and the results summed and divided by the number of theta values. For the seven-hole probe of Figure 3, this process yields

$$\langle C_p \rangle = [1-f-f^2/4+(R')^2] \cos^2\alpha \cos^2\beta - [1+2(R')^2] \tag{10}$$

Huffman developed an expression for a quasi total pressure from his analysis by integrating the pressure over the body surface, resolving this force into an axial component, and dividing by the cross sectional area. His relationship is

$$\langle C_p \rangle_z = -\frac{\cos^2\alpha \cos^2\beta}{R_\ell^2} \int_0^\ell (R^2)' [f+f^2/4+(R')]dz - \sin^2\beta - \sin^2\alpha \cos^2 \tag{11}$$

where ℓ denotes the integration length.

For a conical shaped body, R' is constant and Equation 11 reduces to

$$\langle C_p \rangle_z = [1-f-f^2/4-(R')^2] \cos^2\alpha \cos^2\beta - 1 \tag{12}$$

A probe pressure coefficient that is proportional to the dynamic pressure can be obtained by subtracting Equation 12 from Equation 10 and the dynamic pressure coefficient is

$$\langle C_p \rangle_z - \langle C_p \rangle = 2(R')^2 [1-\cos^2\alpha \cos^2\beta] \tag{13}$$

Some insight into probe calibration can be obtained by studying the plot of α and β versus ΔC_α and ΔC_β in Figure 5, the plot of $\langle C_p \rangle$ versus α and β in Figure 6, the plot of $\langle C_p \rangle_z$ versus α and β in Figure 7, and the plot of $\left[\langle C_p \rangle_z - \langle C_p \rangle \right]$ versus α and β in Figure 8. Figures 5 through 8 were calculated for $R' = .268$ and $f = 0$. Note the near linear relation between each angle and its respective pressure coefficient as shown in Figure 5. Also, the nearly circular contours of constant $\langle C_p \rangle$, $\langle C_p \rangle_z$, and $\left[\langle C_p \rangle_z - \langle C_p \rangle \right]$ as shown in Figures 6, 7, and 8, respectively. Probe manufacturing imperfection and angular misalignment of the pressure ports will cause these curves to become somewhat distorted.

12
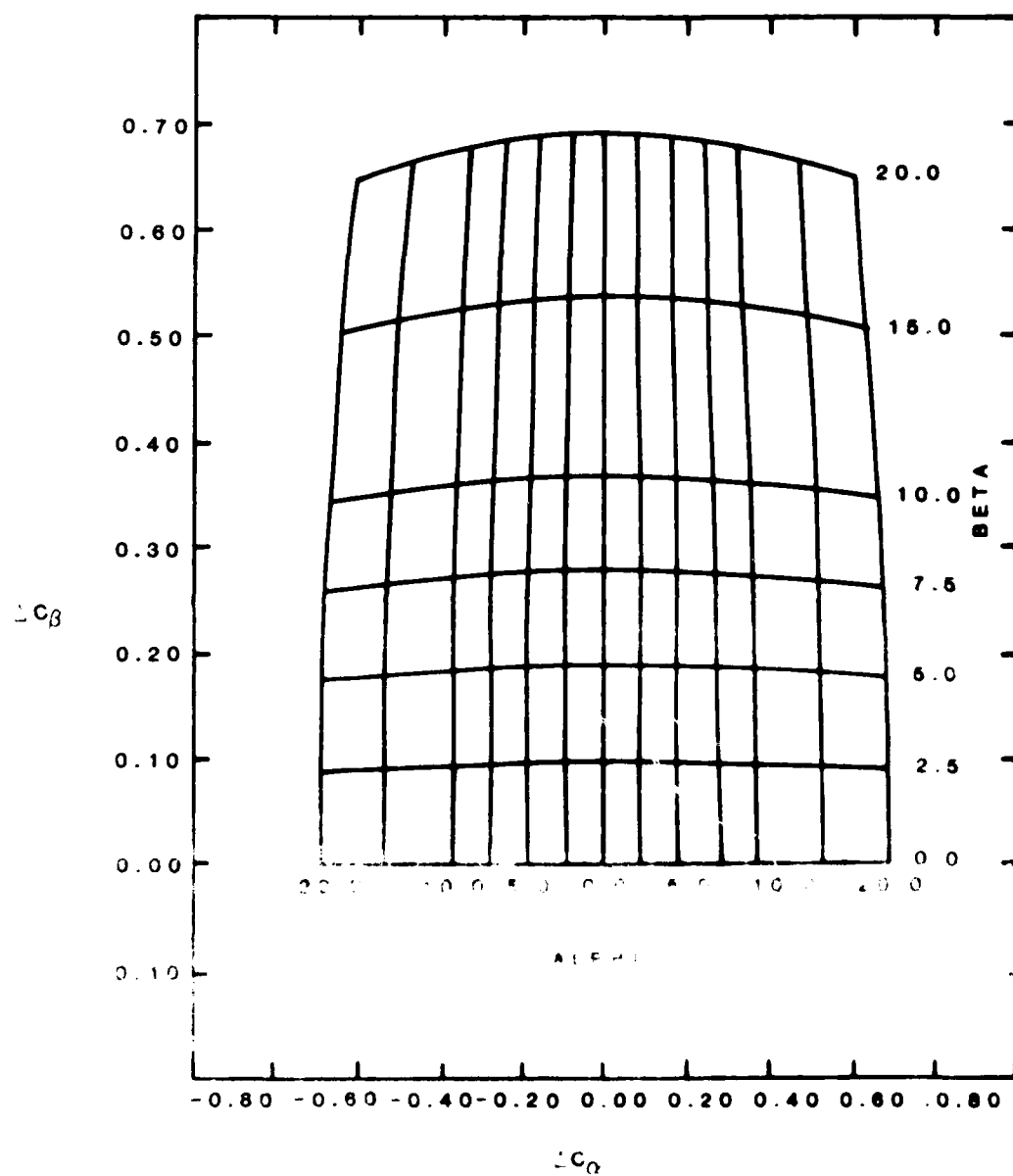
Figure 5. c_β VERSUS c_α FOR A TYPICAL FLOW DIRECTION PROBE (REF 18)

CONTOURS OF CONSTANT <C$_p$>
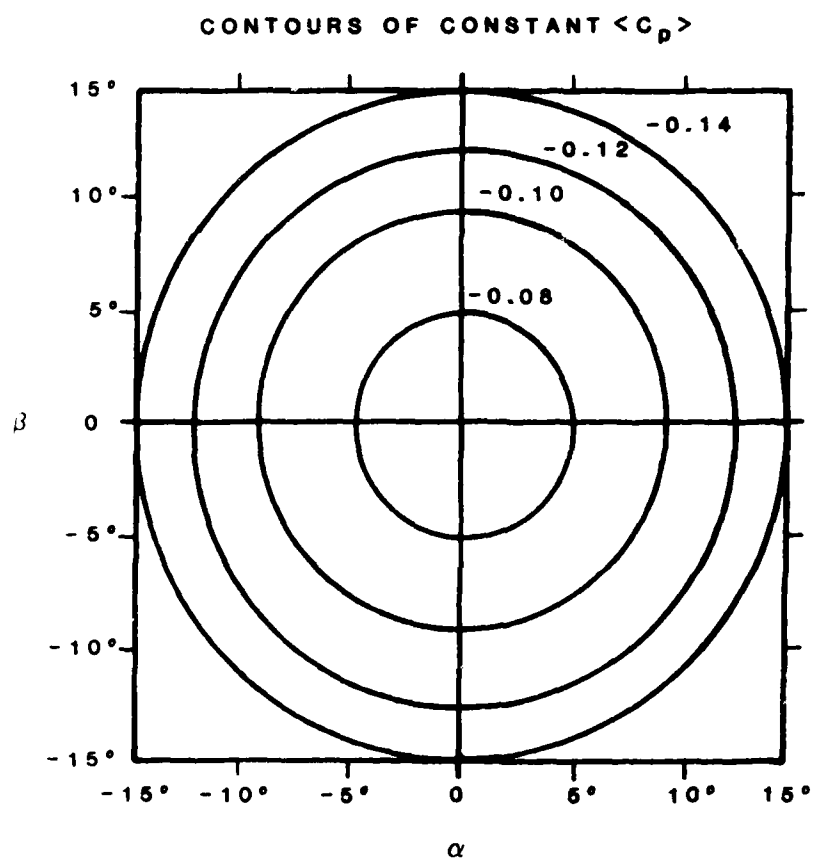
Figure 6. CONTOURS OF CONSTANT<C$_p$>

14

CONTOURS OF CONSTANT$<c_p>_z$
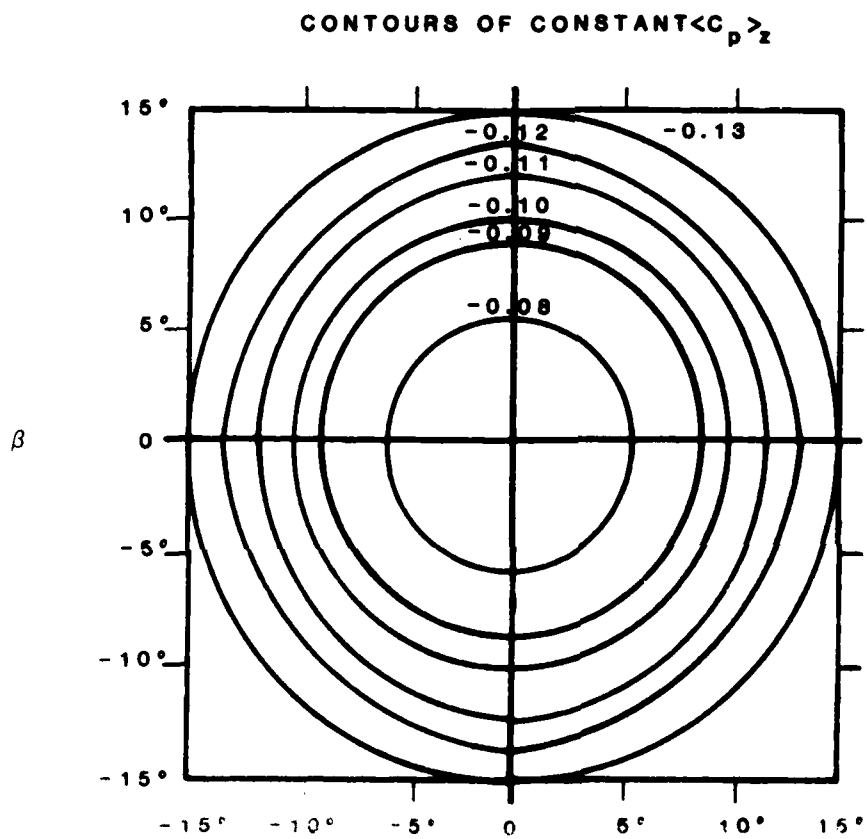
Figure 7. CONTOURS OF CONSTANT$<c_p>_z$

CONTOURS OF CONSTANT $[<C_p>_z - <C_p>]$
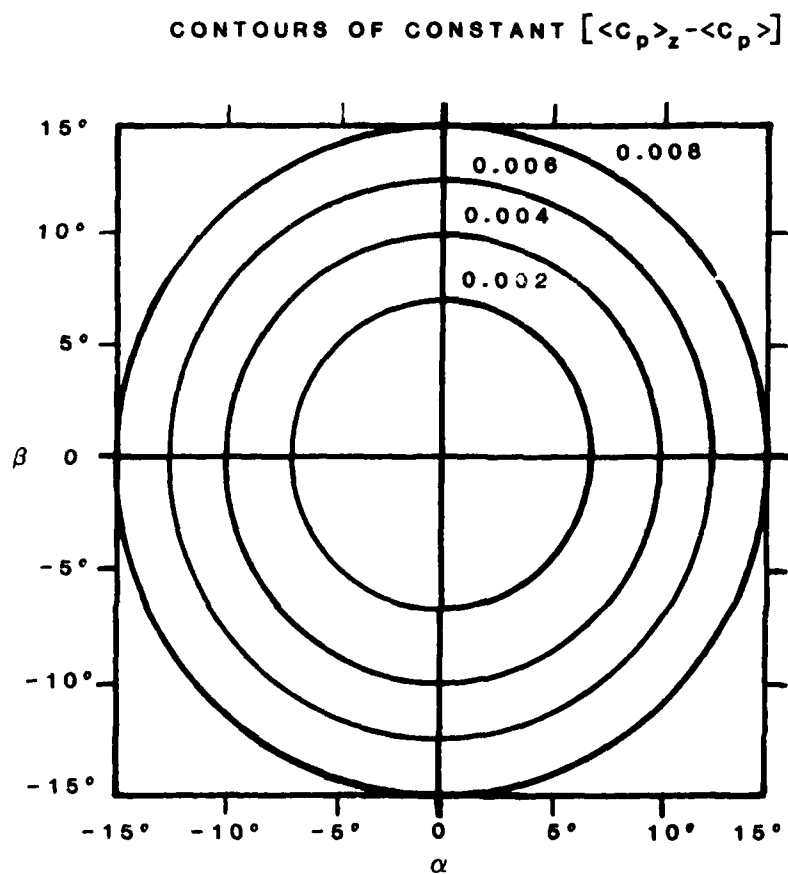
Figure 8. CONTOURS OF CONSTANT $<C_p>_z - <C_p>$

16

C.   Seven-Hole Probe Design

The seven-hole probe is characterized by six periphery ports surrounding one central port (Fig. 9). The probe is constructed by packing seven properly sized stainless steel tubes into a stainless steel casing. For the current probe used at the Air Force Academy, the inner seven tubes have an outside diameter of .023 inches with a .005-inch wall thickness. Once assembled in the order shown below, the tubes are soldered together and machined to the desired half angle ϵ (usually 25 or 30 degrees) at the tip (Ref. 2). It should be noted that the manufacture of seven-hole probes (versus four/five hole probes) is much simpler due to this packing arrangement.
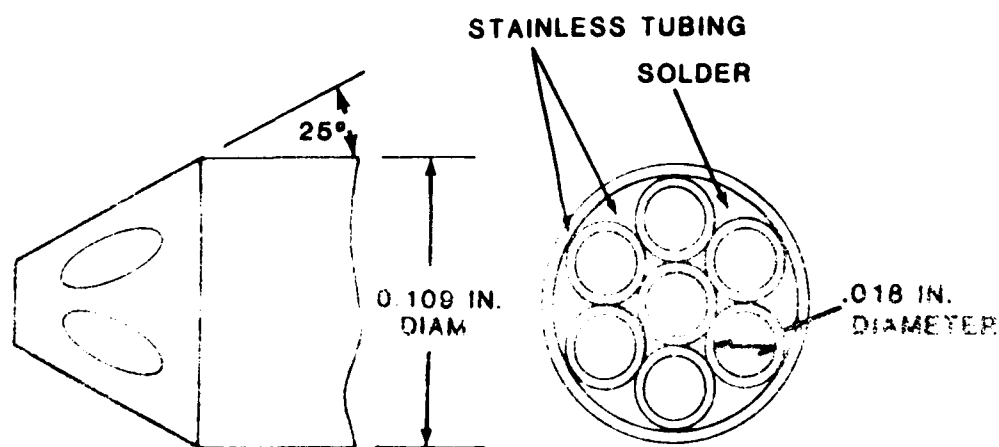
Figure 9. PROBE GEOMETRY

III. Seven-Hole Probe Calibration Theory

Because of their small size and individual construction, all probes have inherent manufacturing defects that require the unique calibration of each probe. Gallington (Ref. 24) developed the calibration theory required for incompressible, uniform flows. His power series method produces explicit polynominal expressions for the desired aerodynamic properties and is easily programmed. The following section presents a synopsis of Gallington's scheme for incompressible, uniform flow calibration as presented by Gallington (Ref. 24) and by Gerner and Maurer (Ref 2).

A. Low Versus High Flow Angles, Incompressible Flow

In this calibration technique for incompressible, uniform flow, the probe face is divided into two sectors. The inner flow sector deals with low flow angles in which the angle between the probe's axis and the freestream velocity vector is less than 30 degrees. The other or outer sector deals with high flow angles of over 30 degrees. Thirty degrees is the dividing point because flow typically begins to detach over the top surface of the probe tip around this local flow angle. The hole numbering system used for both sectors and the remainder of the report is as follows:

FRONT VIEW   SIDE VIEW
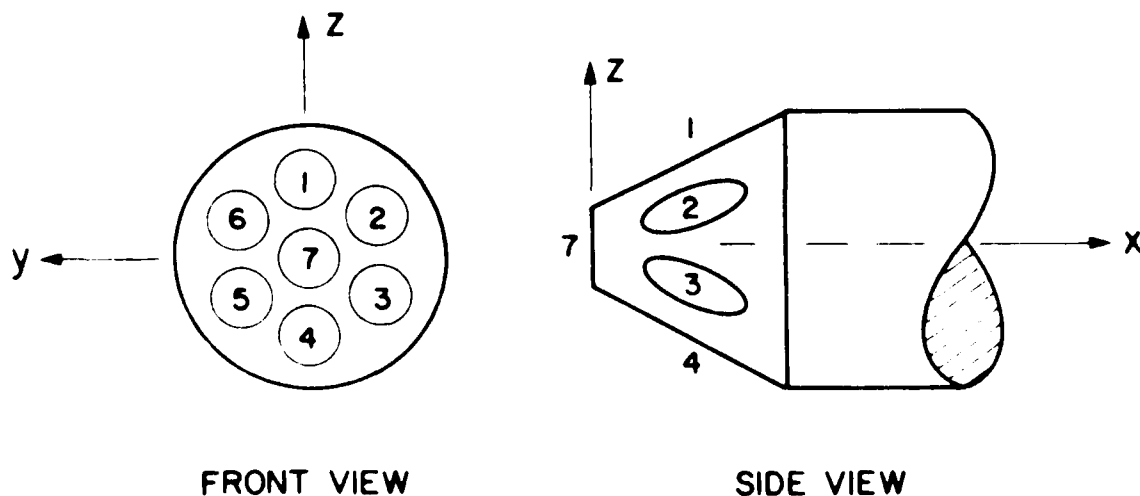
Figure 10. PORT NUMBERING CONVENTION AND PRINCIPAL AXES

18

The x-axis is defined to be positive in the unperturbed freestream flow direction. The origin is a point at the tip of the cone formed by the probe (Fig. 10).

B. Probe Axis System for Low Flow Angles

The axis system for low flow angles is the tangential alpha-beta system depicted below (Fig. 11). The angle of attack, alpha (α_T), is measured directly as the projection on the x-plane. To preserve symmetry, the angle of sideslip (β_T) is measured directly as the projection on the y-plane.
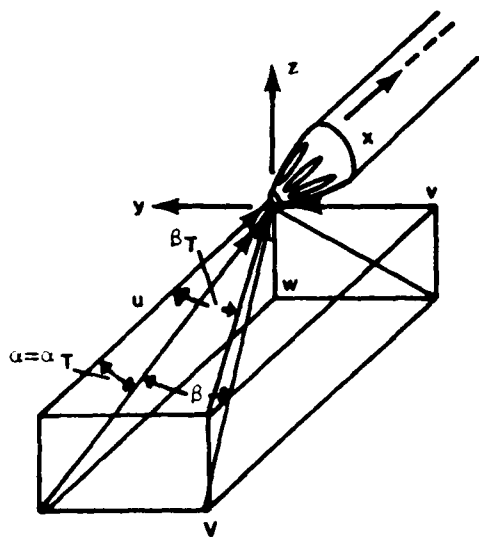
CONVENTIONAL	TANGENT
$u = V \cos\alpha \cos\beta$	$\alpha_T = \arctan \dfrac{w}{u}$
$v = V \sin\beta$	
$w = V \sin\alpha \cos\beta$	$\beta_T = \arctan \dfrac{v}{u}$

Figure 11. LOW ANGLE REFERENCE SYSTEM

1. Pressure Coefficients for Low Flow Angle

The flow angle is determined as a function of dimensionless pressure coefficients. Three pairs of opposing peripheral ports measure the differences in pressure from one side of the probe to the other and form the following three relationships:

$$C_1 = \frac{P_4 - P_2}{P - \bar{P}_{1-6}} \quad , \quad C_{12} = \frac{P_3 - P_1}{P_7 - \bar{P}_{1-6}} \quad , \quad = \frac{P_2 - P_5}{P_7 - \bar{P}_{1-6}}$$

As the numerator measures changes in flow angularity, the denominator nondimensionalizes the expression with the apparent dynamic pressure. The center port pressure, P_7, approximates the local total pressure while the average of the circumferential port pressures $\overline{P}_{1-6}$ approximates the local static pressure. To transform these pressure coefficients to the tangential reference system, Gallington (Ref. 24) formulates the following relationships:

$$C_\alpha = \frac{1}{3}\,(2C_{\alpha_1} + C_{\alpha_2} - C_{\alpha_3}) \qquad , \qquad C_\beta = \frac{1}{\sqrt{3}}\,(C_{\alpha_2} + C_{\alpha_3}) \tag{15}$$

It is important to realize that $C\alpha$ and $C\beta$ are not independent of each other; that is, $C\alpha$ is a function of all six peripheral ports while $C\beta$ is a function of all but ports 1 and 4.

Besides the two angular pressure coefficients, two other low angle pressure coefficients, C_O and C_q, are defined in Gallington's work (Ref. 24):

$$C_O = \frac{P_7 - P_{oL}}{P_7 - \overline{P}_{1-6}} \qquad\qquad C_q = \frac{P_7 - \overline{P}_{1-6}}{P_{oL} - P_{\infty L}} \tag{16}$$

C_O is the apparent total pressure coefficient with respect to each hole and is a means to convert actual pressures measured by the probe to accurate values of local total pressure. The numerator measures the difference between the approximate total pressure measured by the center port P_7 and the actual local total pressure P_{oL}. As with the previous coefficients, the denominator nondimensionalizes the expression with the apparent local dynamic pressure.

The velocity pressure coefficient, C_q, serves a similar conversion function as C_O except that it relates the probe

20

pressures to the actual dynamic pressure. The numerator in this coefficient represents the probe's approximation of the local dynamic pressure while the denominator represents the actual dynamic pressure of the freestream test conditions.

b. Probe Axis System for High Flow Angles

The real advantage of using the non-nulling seven-hole probe over other multi-hole probes appears in the ability to measure high-angle flows. At high angles of attack (greater than 30 degrees), the flow detaches over the upper surface of the probe, and pressure ports in the separated wake are insensitive to small changes in flow angularity (Fig. 12).
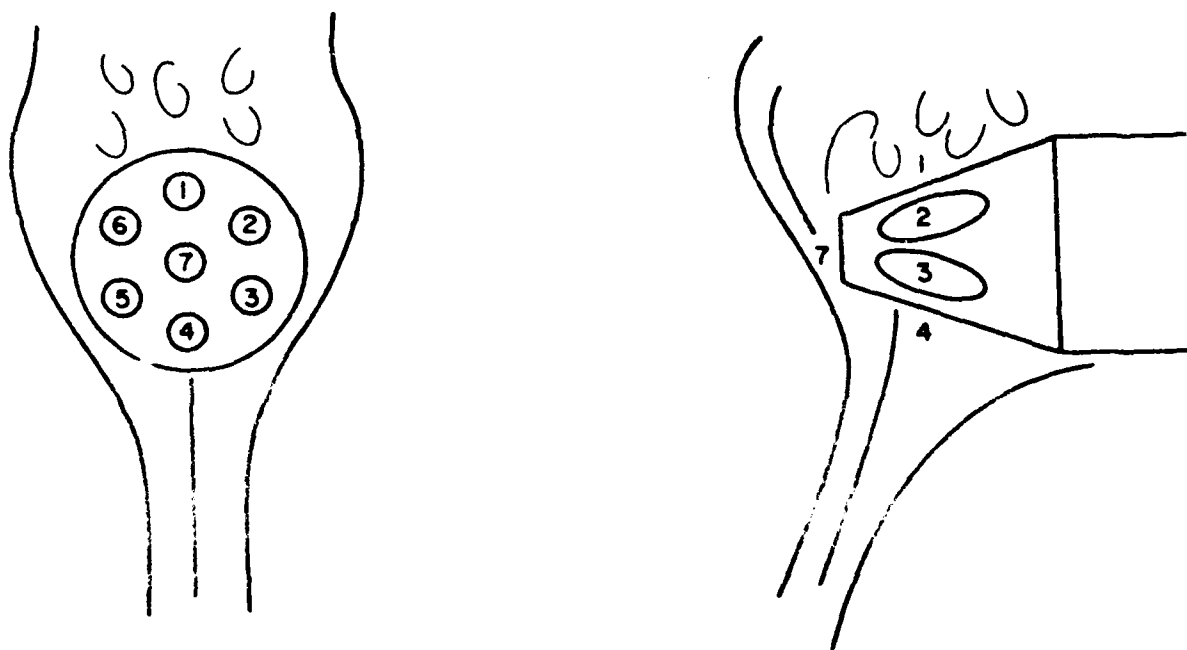

Figure 12. FLOW PATTERN OVER SEVEN-HOLE PROBE
AT HIGH ANGLE OF ATTACK

Consequently, high angle measurements must only be made from ports in the attached flow. Five-hole and other pressure probes have been ineffective in this regime due to this flow separation and lack of sensing ports in the attached flow region. The seven-hole probe avoids this problem because at least three ports remain in the attached flow region, allowing sufficient data to be recorded to document the flow angle.

According to Gallington, the tangential reference system is inappropriate at high flow angles because of indeterminate angles and singularities (Ref. 24). Instead, the polar reference system is used (Fig. 13) where θ represents the pitch angle and ϕ represents the roll angle.
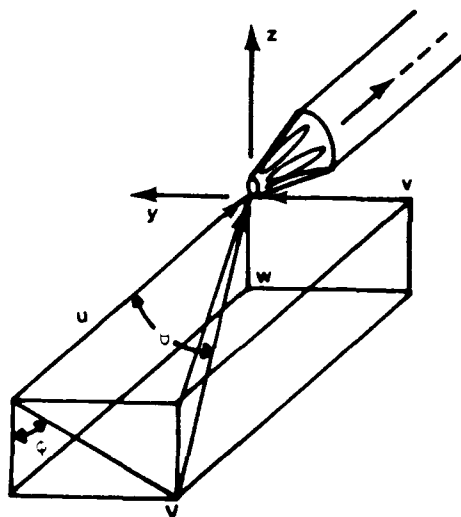
POLAR	TANGENT
$u = V \cos \theta$	$u_T = \arctan \dfrac{w}{u}$
$v = V \sin\theta \sin\phi$	$r_T = \arctan \dfrac{v}{u}$
$w = V \sin\theta \cos\phi$	

Figure 13. HIGH ANGLE REFERENCE SYSTEM

More specifically, θ denotes the angle that the velocity vector forms with respect to the probes's x-axis, and ϕ signifies the azimuthal orientation of the velocity vector in the y-z plane. We should note that a positive ϕ is measured counterclockwise from the the negative z axis when the probe is viewed from the front.

22

Based on Gallington's original work with the seven-hole probe at high angles of attack, Gerner and Mauer accomplished the following analysis (Ref 2). Kuethe and Chow's Foundations of Aerodynamics: Bases of Aerodynamic Design, explains that the separation points of a cylinder in turbulent flow are over 100 degrees from the frontal stagnation point. Flow around a conical body such as a probe tip was likely to remain attached longer, and the u-velocity component was prone to extend the separation points downstream even further. Therefore, for the high angle flow shown in Figure 14, ports 3, 4, 5, and 7 lie in attached flow, and port 1 lies in separated flow. The flow over ports 2 and 6 is unpredictable, and their readings are discarded (Ref. 2).
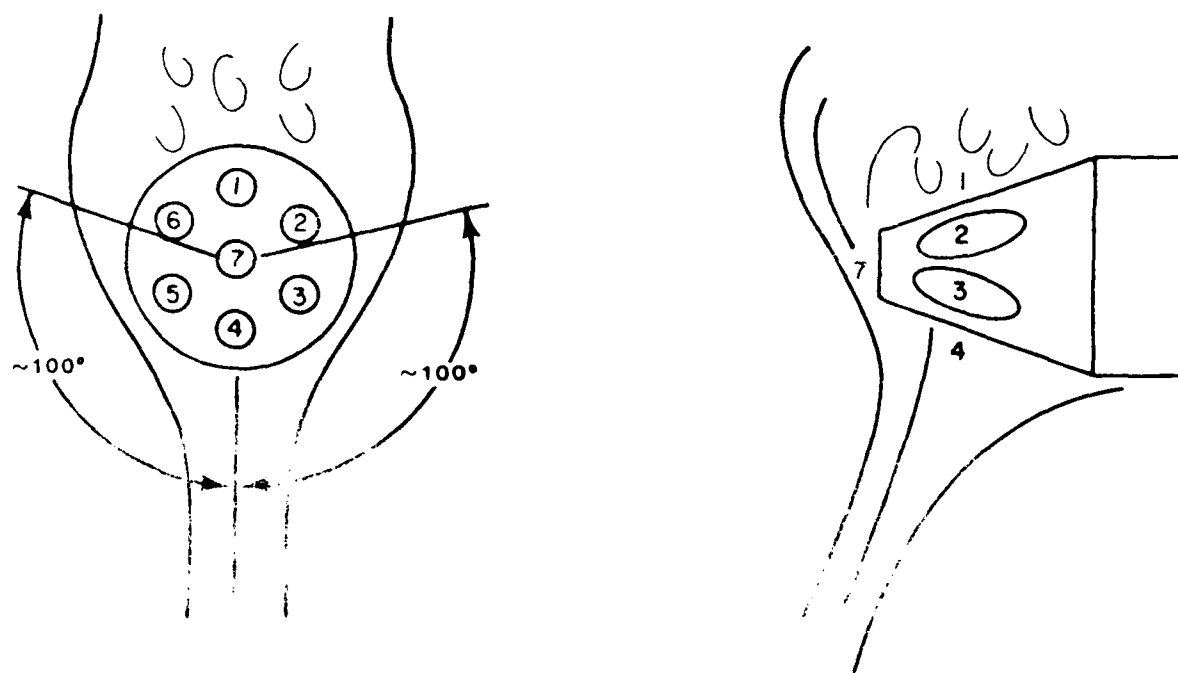

Figure 14. FLOW OVER PROBE AT HIGH ANGLE OF ATTACK

... Data ... for High Flow Angles

... boundaries, high flow angles ...

pressure differences. Unlike low flow angles, however, the center port pressure is now the most dependent port on local flow angle. Consequently, a pitch angular pressure coefficient should measure the difference between the center port and a new stagnation port. In the example below, the pressure at P_4 approximates the local total pressure.

$$C_{O_4} = \frac{P_4 - P_7}{P_4 - \dfrac{P_3 + P_5}{2}} \qquad (17)$$

The expression is again nondimensionalized by the apparent dynamic pressure. The average of P_3 and P_5 approximates the static pressure and is relatively independent to changes in roll.

Although the average is independent of ϕ, the difference is sensitive to roll angle. As the probe's azimuthal orientation changes, the windward pressure rises and the leeward pressure falls. The result is a roll angular pressure coefficient (example for port 4 is Equation 8 below) that is also nondimensionalized by the apparent dynamic pressure.

$$C_{\phi_4} = \frac{P_3 - P_5}{P_4 - \dfrac{P_3 + P_5}{2}} \qquad (18)$$

The high flow-angle C_O and C_q coefficients are translated from their low flow angle counterparts using the same rationale found in the development of C_ψ and C_ϕ. The low-angle C_O and C_q coefficients are changed to account for the different ports that represent total and static pressures in the high-angle regime. The equations for C_ψ, C_ϕ, C_O, and C_q are as follows:

24

$$C_{\Theta_1} = \frac{P_1 - P_7}{P_1 - \frac{P_2 + P_6}{2}} \quad , \qquad C_{\phi_1} = \frac{P_6 - P_2}{P_1 - \frac{P_6 + P_2}{2}}$$

$$C_{\Theta_2} = \frac{P_2 - P_7}{P_2 - \frac{P_1 + P_3}{2}} \quad , \qquad C_{\phi_2} = \frac{P_1 - P_3}{P_2 - \frac{P_1 + P_3}{2}}$$

$$C_{\Theta_3} = \frac{P_3 - P_7}{P_3 \frac{P_2 + P_4}{2}} \quad , \qquad C_{\phi_3} = \frac{P_2 - P_4}{P_3 - \frac{P_2 + P_4}{2}}$$

$$(19)$$

$$C_{\Theta_4} = \frac{P_4 - P_7}{P_4 = \frac{P_3 + P_5}{2}} \quad , \qquad C_{\phi_4} = \frac{P_3 - P_5}{P_4 - \frac{P_3 + P_5}{2}}$$

$$C_{\Theta_5} = \frac{P_5 - P_7}{P_5 - \frac{P_4 + P_6}{2}} \quad , \qquad C_{\phi_5} = \frac{P_4 - P_6}{P_5 - \frac{P_4 + P_6}{2}}$$

$$C_{\Theta_6} = \frac{P_6 - P_7}{P_6 - \frac{P_5 + P_1}{2}} \quad , \qquad C_{\phi_6} = \frac{P_5 - P_1}{P_6 - \frac{P_5 + P_1}{2}}$$

$$C_{o_1} = \frac{P_1 - P_{oL}}{P_1 - \dfrac{P_2 + P_6}{2}}$$

$$C_{q_1} = \frac{P_1 - \dfrac{P_2 + P_6}{2}}{P_{oL} - P_{\infty L}}$$

$$C_{o_2} = \frac{P_2 - P_{oL}}{P_2 - \dfrac{P_3 + P_1}{2}}$$

$$C_{q_2} = \frac{P_2 - \dfrac{P_3 + P_1}{2}}{P_{oL} - P_{\infty L}}$$

$$C_{o_3} = \frac{P_3 - P_{oL}}{P_3 - \dfrac{P_4 + P_2}{2}}$$

$$C_{q_3} = \frac{P_3 - \dfrac{P_4 + P_2}{2}}{P_{oL} - P_{\infty L}}$$

$$C_{o_4} = \frac{P_4 - P_{oL}}{P_4 - \dfrac{P_5 + P_3}{2}}$$

$$C_{q_4} = \frac{P_4 - \dfrac{P_5 + P_3}{2}}{P_{oL} - P_{\infty L}}$$

$$C_{o_5} = \frac{P_5 - P_{oL}}{P_5 - \dfrac{P_6 + P_4}{2}}$$

$$C_{q_5} = \frac{P_5 - \dfrac{P_6 + P_4}{2}}{P_{oL} - P_{\infty L}}$$

$$C_{o_6} = \frac{P_6 - P_{oL}}{P_6 - \dfrac{P_1 + P_5}{2}}$$

$$C_{q_6} = \frac{P_6 - \dfrac{P_1 + P_5}{2}}{P_{oL} - P_{\infty L}}$$

(20)

26

F. Division of Angular Space

The most obvious difference between low and high pressure coefficients is that six high coefficients are needed for the high angles. This fact leads to the question of what factors determine when a certain set of coefficients should be employed. Gallington proposes the "division of angular space" shown in Figure 15 (Ref. 24).
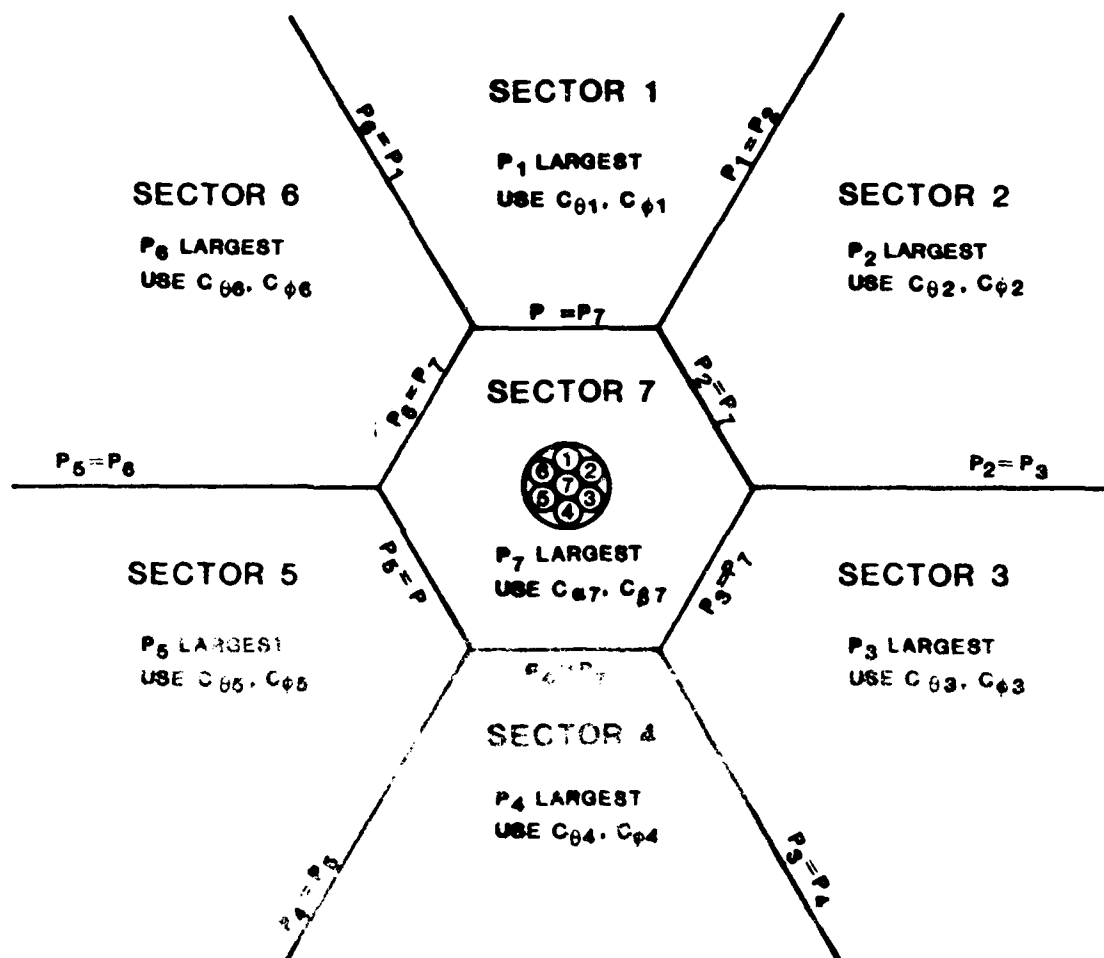

Figure 15. DIVISION OF ANGULAR SPACE

This method separates probe measurements into seven sectors -- a central low angle sector and six circumferential high angle sectors. Data points are placed in a given sector based on the highest port pressure measured on the probe.

G.   Polynomial Power Series Expansion

Once the pressure coefficients are calculated, they must be converted to α_T, β_T, C_O, or C_q for low angle flows and θ, ϕ, C_O, or C_q for high angle flows. This conversion is accomplished by solving the following fourth order power series:

Order of Terms

$$A_i = K_1^A +$$ \qquad\qquad\qquad\qquad 0th

$$K_2^A C_{\alpha_i} + K_3^A C_{\beta_i} +$$ \qquad\qquad 1st

$$K_4^A C_{\alpha_i}^2 + K_5^A C_{\alpha_i} C_{\beta_i} + K_6^A C_{\beta_i}^2 +$$ \qquad 2nd \qquad (21)

$$K_7^A C_{\alpha_i}^3 + K_8^A C_{\alpha_i}^2 C_{\beta_i} + K_9^A C_{\alpha_i} C_{\beta_i}^2 + K_{10}^A C_{\beta_i}^3 +$$ \qquad 3rd

$$K_{11}^A C_{\alpha_i}^4 + K_{12}^A C_{\alpha_i}^3 C_{\beta_i} + K_{13}^A C_{\alpha_i}^2 C_{\beta_i}^2 + K_{14}^A C_{\alpha_i} C_{\beta_i}^3 + K_{15}^A C_{\beta_i}^4$$ \qquad 4th

"A" signifies the desired output quantity with the subscript denoting the ith such quantity. "K" denotes the presently unknown calibration coefficients. The calibration process entails finding these calibration coefficients with the A's as known conditions and the C's as measured pressure coefficients at these known conditions.

28

B.   Determination of Calibration Coefficients

Rewriting in matrix notation for n terms, the power series becomes

$$
\begin{bmatrix} A_1 \\ A_2 \\ A_3 \\ \cdot \\ \cdot \\ \cdot \\ A_n \end{bmatrix} = \begin{bmatrix} 1 & C_{\alpha_1} & C_{\beta_1} & C^2_{\alpha_1} & C_{\alpha_1} & C_{\beta_1} & C^2_{\beta_1} & \cdots & \cdots & C^4_{\beta_1} \\ 1 & C_{\alpha_2} & C_{\beta_2} & C^2_{\alpha_2} & C_{\alpha_2} & C_{\beta_2} & C^2_{\beta_2} & \cdots & \cdots & C^4_{\beta_2} \\ 1 & C_{\alpha_3} & C_{\beta_3} & C^2_{\alpha_3} & C_{\alpha_3} & C_{\beta_3} & C^2_{\beta_3} & \cdots & \cdots & C^4_{\beta_3} \\ \cdot & \cdot & \cdot & \cdot & \cdot & \cdot & \cdot & & & \cdot \\ \cdot & \cdot & \cdot & \cdot & \cdot & \cdot & \cdot & & & \cdot \\ \cdot & \cdot & \cdot & \cdot & \cdot & \cdot & \cdot & & & \cdot \\ 1 & C_{\alpha_n} & C_{\beta_n} & C^2_{\alpha_n} & C_{\alpha_n} & C_{\beta_n} & C^2_{\beta_n} & \cdots & \cdots & C^4_{\beta_n} \end{bmatrix} \begin{bmatrix} K^A_1 \\ K^A_2 \\ K^A_3 \\ \cdot \\ \cdot \\ \cdot \\ K^A_{15} \end{bmatrix}
$$

(22)

or simply

$$[A] = [C][K]$$

(23)

Solving for $[K]$ by the least squares curve fit outlined by Netter and Wasserman in Gallington (Ref. 24), the following is obtained:

$$[K] = [C^T C]^{-1}[C]^T[A]$$

(24)

With known calibration coefficients, the probe can be used to determine output quantities (α, β, ..., C_p, ..., ϕ, ...) α, β, ... for an unknown flow field. It is important to note here that to this point the flow field has been uniform and steady. ..... Temperature or velocity gradients have not been accounted for. Finally, while the local total and dynamic pressures are not found explicitly from the power series, ... are

easily determined by substituting C_0 and C_q into Equation 16 (low angles) or Equation 20 (high angles).

I. Extension to Compressible Flows

Gerner and Maurer (Ref. 2) expanded the technique to subsonic compressible flows with the introduction of a nondimensional pressure coefficient representative of compressibility effects. This coefficient, C_M, had to become insignificant at very low Mach numbers; thus, any terms bearing C_M in the power series expansion would have to approach zero as Mach approached zero. This would leave essentially an incompressible power series with the regular two angular pressure coefficients as previously described. Because pressure probes are unable to determine Mach number in the hypersonic range, C_M had to approach a finite limit at very high Mach numbers. Consequently, large changes of Mach numbers in this region would have negigible effect on the compressibility coefficient.

Gerner and Maurer (Ref. 2) found that these requirements were satisfied by the apparent dynamic-to-total-pressure ratio (low angles).

$$C_M = \frac{P_7 - \overline{P}_{1-6}}{P_7} \tag{25}$$

Similarly, for high angle flow, the compressibility coefficient in each sector is:

$$C_{M_1} = \frac{P_1 - \dfrac{P_6 + P_2}{2}}{P_1} \qquad\qquad C_{M_4} = \frac{P_4 - \dfrac{P_3 + P_2}{2}}{P_4}$$

$$C_{M_2} = \frac{P_2 - \dfrac{P_1 + P_3}{2}}{P_2} \qquad\qquad C_{M_5} = \frac{P_5 - \dfrac{P_4 + P_6}{2}}{P_5}$$

$$C_{M_3} = \frac{P_3 - \dfrac{P_2 + P_4}{2}}{P_3} \qquad\qquad C_{M_6} = \frac{P_6 - \dfrac{P_5 + P_1}{2}}{P_6}$$

One of the primary problems of extending the seven-hole probe's capabilities into compressible flow lies in the mathematics. First, by adding a third coefficient to the fourth order power series, the number of terms and hence calibration coefficients jumps from 15 to 35. Gerner and Mauer say that approximately 80 data points in two variables (C_α and C_β) for each of the seven sectors are needed for a complete incompressible calibration. That fact results in 560 data points, and the addition of a Mach number compressibility coefficient makes the data set unwieldy (Ref. 2). These two factors create complex and time consuming matrix operations. Additionally, the amount of run time needed to operate the wind tunnel for all of the calibration data points is prohibitive as well as costly.

Gerner and Maurer suggest a two-part solution to make the addition of C_M feasible. By reducing the fourth order power series to a third order, the number of calibration coefficients is reduced to 20. Gerner and Maurer also decrease the number of data points required for calibration by employing a 6x6 Latin Square technique (Ref. 2) for purposes of obtaining calibration data. The Latin Square is a numerical method that ensures a homogeneous, random sample of a three-dimensional parametric space.

Seven hole probe work incorporating these two changes results in the following conclusions for compressible flow. The third order polynomial function accurately represents the parameter plane up to incompressible and 70 degrees of pitch. Next, based on statistically significant difference between the standard deviations of compressible calibrations and incompressible calibration, Latin

Squares produce a sample which accurately represents a very large three-dimensional parameter space.

With these changes, the seven-hole probe may now be used in an unknown uniform, compressible flow. Since the seven-hole probe has never been subjected to supersonic applications, no shocks will lie ahead of the probe, and the isentropic flow relationship is employed to find Mach number (Ref. 2).

$$M_\infty = \frac{2}{\gamma - 1} \left(\left[1 - \frac{P_o - P_\infty}{P_o} \right]^{(1-\gamma)/\gamma} - 1 \right) \tag{27}$$

Knowing C_o, C_q, and the seven port pressures, the local Mach number may be determined explicitly from the dynamic to total pressure ratio. This ratio for the inner sector is represented in Equation 28 below (Ref. 2).

$$\frac{P_{oL} - P_{\infty L}}{P_{oL}} = \left[C_q \left(\frac{P_7}{P_7 - P_{1-6}} - C_o \right) \right]^{-1} \tag{28}$$

Similar equations for the outer sectors may be derived, using the appropriate port pressures for approximate total and dynamic pressures.

IV. Seven-Hole Probe in Shear Flow

Under the present calibration scheme, the existence of a velocity gradient in the flow will cause the probe to measure an erroneous uniform flow at fictitious flow angle. For example, a flow having the properties $M = .3, \alpha = 0°, \beta = 0°$, with a velocity gradient (Fig.16) might cause the probe to "think" that it sees a flow with a certain angularity, say $\beta = 10°$ (see Fig. 17).
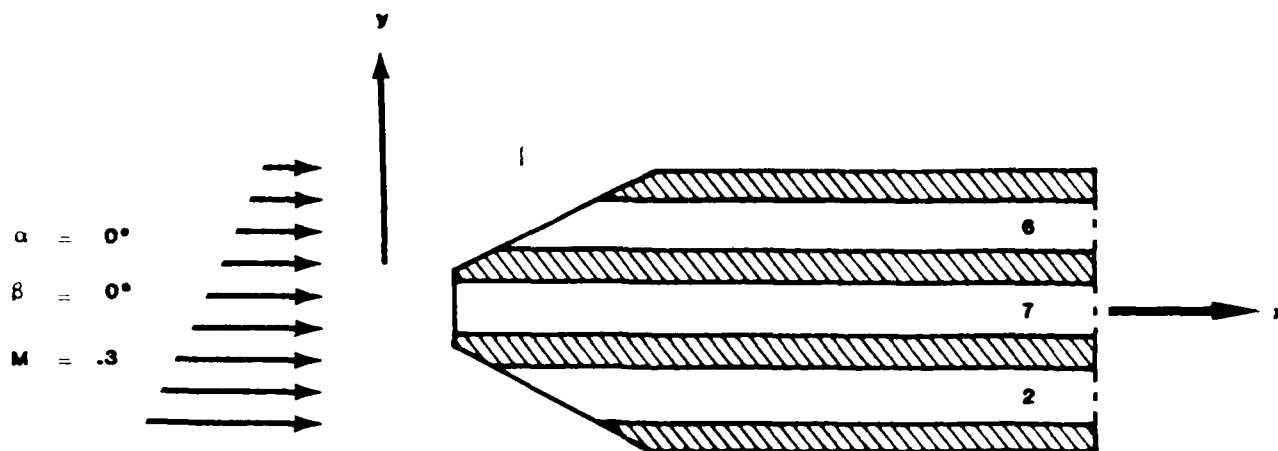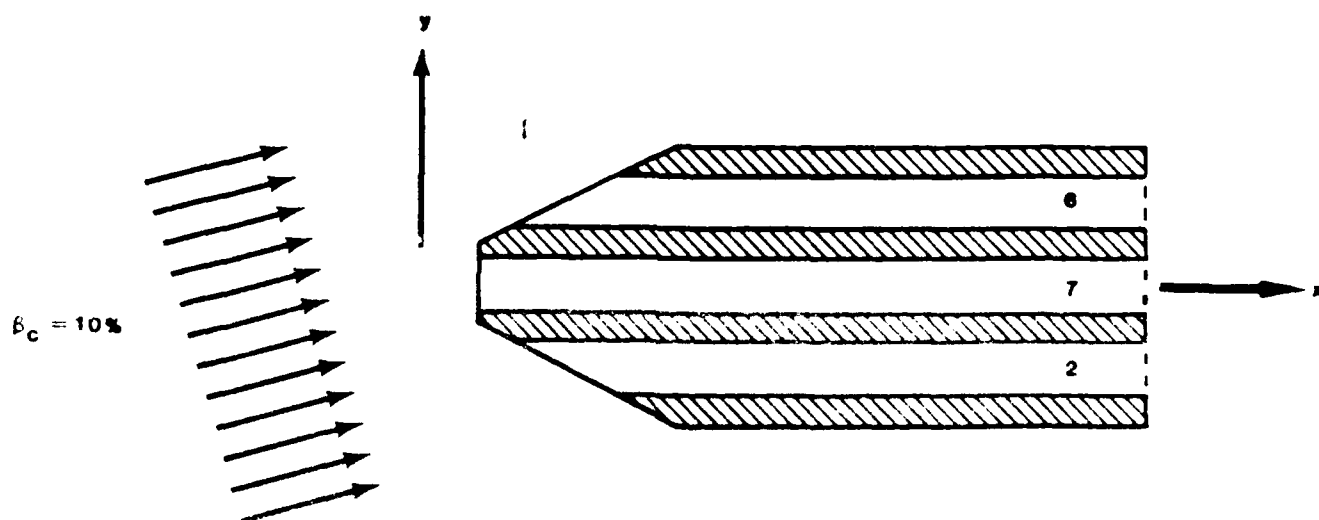
Figure 16. ACTUAL FLOW CONDITION

Figure 17. APPARENT FLOW CONDITION

different a pressure coefficient, all seven values compute a single uniform flow calibration produces an apparent flow condition that

determined. Then using the "backstepping" technique developed in the following sections, the apparent measured values can be corrected to the actual flow values.

A. Slender Body Theory

The slender body theory developed by Huffman is utilized in this section to model flow around the probe (Ref. 20). With this model, the probe's port pressure coefficients can be estimated as a function of flow angularity. Using Huffman's method of viewing the probe as a small perturbation to an otherwise uniform stream, the pressure coefficients are determined by analytic means. Further, the model determines the variation of pressure coefficients with flow direction. Not included are viscous or flow separation effects as the theory is based on potential flow.

The body-geometry function, f, is a parameter used to define the geometric characteristics of a slender body and is given in Equation 2. Huffman incorporates the body shape function into calculations for the pressure coefficient as given by Equation 4. A simplified form of Equation 4 was used in this analysis as given below.

$$
\begin{aligned}
C_{p_{i_c}} = {} & \cos^2 \alpha \cos^2 \beta[-f - (R')^2] + \sin^2 \beta[1 - 4 \sin^2 \theta] \\
& + \sin^2 \alpha \cos^2 \beta[1 - 4 \cos^2 \theta] + \cos \alpha \sin 2\beta[-2R' \cos \theta] \\
& + \sin 2\alpha \cos^2 \beta[-2R' \sin \theta] + \sin 2\alpha \cos \beta(4 \sin \theta \cos \theta)
\end{aligned}
\tag{29}
$$

where R' is dR/dX with R as the radius of the probe, and (θ) is the angle measured from the y-axis to the pressure port in question. The subscript "c" signifies that the approximation is valid for uniform incompressible flow.

34

The function that Huffman develops for the pressure coefficient at port 7 simplifies to Equation 30.

$$C_{p_{7_c}} = \cos^2\alpha \, \cos^2\beta - \sin^2\beta - \sin^2\alpha \, \cos^2\beta \qquad (30)$$

One must realize that slender body theory is only an approximate model of flow around the seven-hole probe. The reason for this use stems from the conditions that the body radius is much less than the body length (slender body), and that it is easily applied to compressible flows. The only problem with this approach is that it assumes that the rate of change of body radius with respect to body length must be small. The seven-hole probe does not completely conform to this assumption for two reasons. First, the probe has a blunt tip with a slope discontinuity, while slender body theory assumes an aerodynamically smooth body coming to a point. Because the tip is blunt, flow disturbances originate at that tip. Second, due to the orientation of the peripheral hole surfaces, separation occurs on the body probe at moderate angles of attack. Slender body theory assumes non-separated flow over the body for all flow angles. Even with these discrepancies, slender body theory is effective in predicting basic trends for coefficient
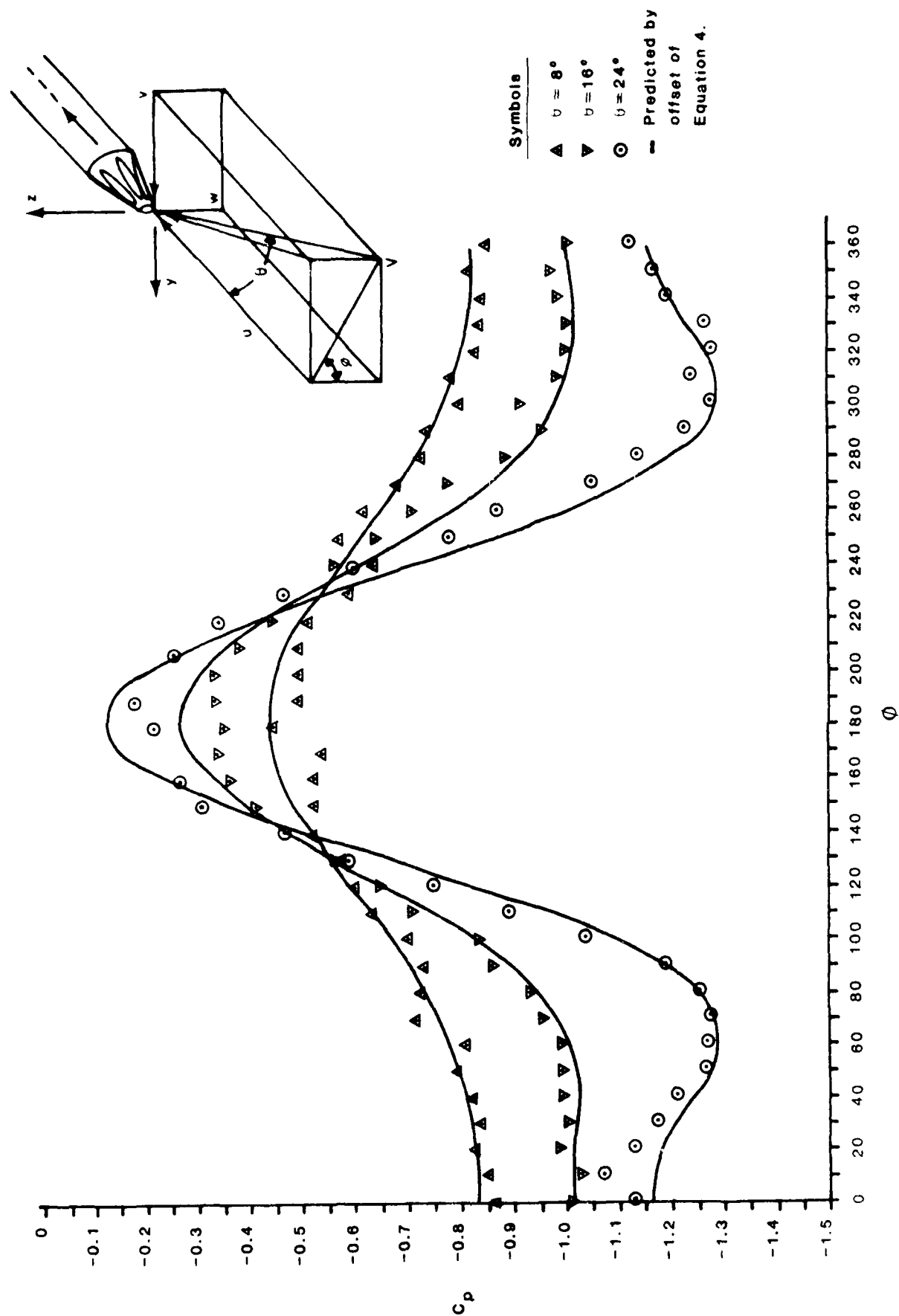
a uniform flow with no flow angularity the

Figure 18. PREDICTED AND MEASURED C_p FOR HOLE # 1

b.   The Shear Gradient

In order to work with a two-dimensional shear gradient, an alpha-beta plane is defined normal to the direction of the actual velocity and through the center point of port number 7 (Fig. 19a). The velocity at port 7 is used as a reference velocity; hence,

normal plane (R)
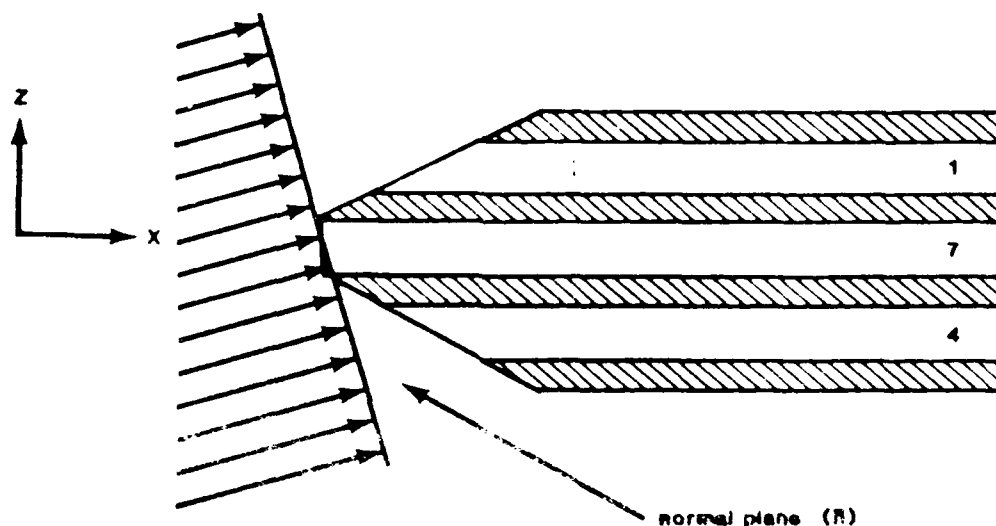
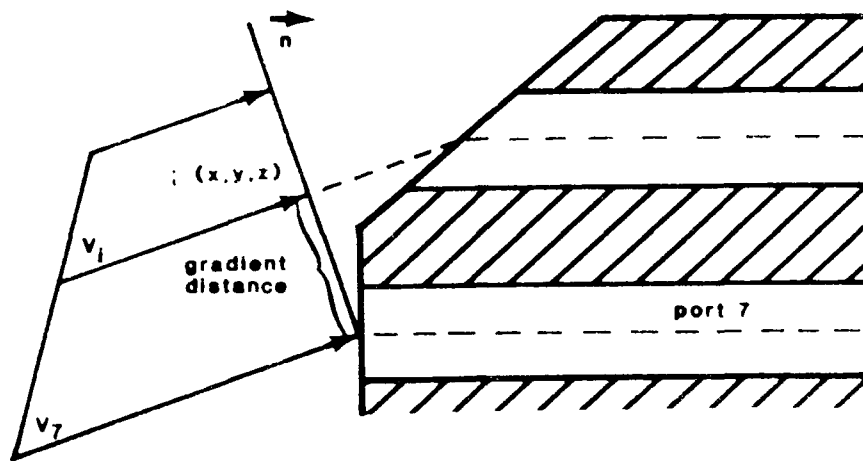**Figure 19a.   SEVEN–HOLE PROBE IN A SHEAR GRADIENT**

Figure 19b. CLOSE-UP OF NORMAL PLANE

By determining this gradient distance, the following general equation can be used to define the gradient's effect on the velocity.

$$V = V_7 + \frac{dV}{dy} y + \frac{dV}{dz} z$$

where y and z are the components of the gradient distance and dV/dz and dV/dy are indicators of the magnitude of the alpha and beta shear gradients respectively. To put this equation in a more usable form, the gradients are non-dimensionalized:

$$V = V_7 \left(1 + \frac{s}{V_7} \frac{dV}{dy} \frac{y}{s} + \frac{s}{V_7} \frac{dV}{dz} \frac{z}{s}\right)$$

where s is the distance between the centers of opposite ports. With this new equation, the terms $\frac{s}{V_7} \frac{dV}{dy}$ and $\frac{s}{V_7} \frac{dV}{dz}$ can be assigned a magnitude of relative gradient.

C. Gradient Effects on Port Pressure Coefficients

For a uniform calibration the pressure at the peripheral holes may be found by the following expression.

$$C_{p_i} = C_{p_{i_c}} \left(1 + \frac{s}{V_7} \frac{dV}{dy} \left(\frac{y}{s}\right) + \frac{s}{V_7} \frac{dV}{dz} \left(\frac{z}{s}\right)\right)^2 \tag{33}$$

Since $C_{p_{i_c}}$ is a uniform coefficient based on the geometry of the slender body theory, V_i is the only term that accounts for gradient effects. Consequently, V_i in shear flow differs for each peripheral hole. If the velocity term is kept constant at V_7 and the gradient effects are accounted for by the coefficients of pressure, the following expression results:

$$P_i = P_\infty + C_{p_{i_c}} \left(\tfrac{1}{2}\rho V_i^2\right) \tag{34}$$

Solving Equations 33 and 34 for C_p, it is evident that pressure is proportional to the square of velocity in incompressible flow.

$$P_i = P_\infty + C_{\bar{p}_i} \left(\tfrac{1}{2}\rho V_7^2\right) \tag{35}$$

The gradient correction

$$\cdots = C_{p_c} \left(\frac{V_i}{V}\right)^2$$

the determination of point (x,y,z). The vector analysis behind the location of point (x,y,z) is explained in detail in Johnson and Reed (Ref. 25). The results are as follows:

$$x = x_1 + (x_7 - x_1)\cos\alpha\cos\beta - \cos\alpha\cos\beta\,[y_1\sin\beta + z_1\sin\alpha\cos\beta]$$

$$y = y_1 + (x - x_1)\tan\beta/\cos\alpha$$

$$z = z_1 + (x - x_1)\tan\alpha$$

(37)

Port (i)	x_1	y_1	z_1
1	$s/2\tan\epsilon$	$(s/2)\cos\theta_1$	$(s/2)\sin\theta_1$
2	$s/2\tan\epsilon$	$(s/2)\cos\theta_2$	$(s/2)\sin\theta_2$
3	$s/2\tan\epsilon$	$(s/2)\cos\theta_3$	$(s/2)\sin\theta_3$
4	$s/2\tan\epsilon$	$(s/2)\cos\theta_4$	$(s/2)\sin\theta_4$
5	$s/2\tan\epsilon$	$(s/2)\cos\theta_5$	$(s/2)\sin\theta_5$
6	$s/2\tan\epsilon$	$(s/2)\cos\theta_6$	$(s/2)\sin\theta_6$
7	$d/2\tan\epsilon$	0	0

Since x_i, y_i, z_i, and x_7 are known values, the knowledge of alpha and beta will locate the point (x,y,z).

E. Shear Flow Measurement Corrections

At this point, the mathematical relationships necessary to compare the effects of velocity gradients are available. Equation 15 provides the ability to calculate C_α, C_{α_c}, and C_β, and C_{β_c}, realizing that

$$C_{\alpha_1} = \frac{P_4 - P_1}{P_7 - \overline{P}_{1-6}} = \frac{C_{p_4} - C_{p_1}}{C_{p_7} - C_{p_{1-6}}} \qquad C_{\alpha_3} = \frac{P_3 - P_5}{P_7 - P_{1-6}} = \frac{C_{p_3} - C_{p_5}}{C_{p_7} - C_{p_{1-6}}}$$

$$C_{\alpha_2} = \frac{P_3 - P_6}{P_7 - \overline{P}_{1-6}} = \frac{C_{p_3} - C_{p_6}}{C_{p_7} - C_{p_{1-6}}}$$

39

By comparing the actual to the apparent angular pressure coefficients, the actual angles can be incremented until the apparent and actual coefficients are equal. This procedure indicates the flow angle errors inherent in the measurement of velocity gradients.

In order to determine the effects of different shear gradients at varying alphas and betas, Johnson and Reed (Ref. 25) calculated the apparent flow angles resulting from a span of actual flow angles and shear gradients. The calculations show the errors between the apparent angles and actual input values. Consequently, the actual flow angles can be determined by backstepping from the apparent angles. Although these calculations only allow manual corrections to apparent measurements, the theory of this section can be used to generate a family of data points. These points may then be input into a computer surface fitting scheme for highly accurate, near real-time correction to the apparent data.

## 7. Seven-Hole Probe Measurement Capabilities

Three key elements of the seven-hole probe's measurement effectiveness in unknown flows are discussed further in order to provide an understanding of the basics behind its actual and potential capabilities. The three elements to be discussed are the probe's calibration, construction, and measurement error.

a. Calibration.

Every probe must be uniquely calibrated due to manufacturing imperfections. The specifics of the seven-hole probe's calibration have been outlined in past sections. The process of calibrating the multihole

probes, seven-hole probe calibration allows for the relative flow angles, total pressure, and static pressure to be determined explicitly. With computer processing, these calculations are performed in near real time.

As discussed earlier, problems with the present calibration arise when attempting to make measurements in shear flow. This is because the present calibration and associated calibration coefficients are determined in a uniform flow. Jonas recorded measurement discrepancies in his attempts to use the seven-hole probe to map unknown flow fields with suspected shear (Ref. 26). Specifically, he compared seven-hole and total pressure probe measurements in a vortex wake created by the wing leading-edge extensions of a Northrop VATOL model.

TOP VIEW

10 in

HRL   HRL

|← 15.35 in →|

SIDE VIEW
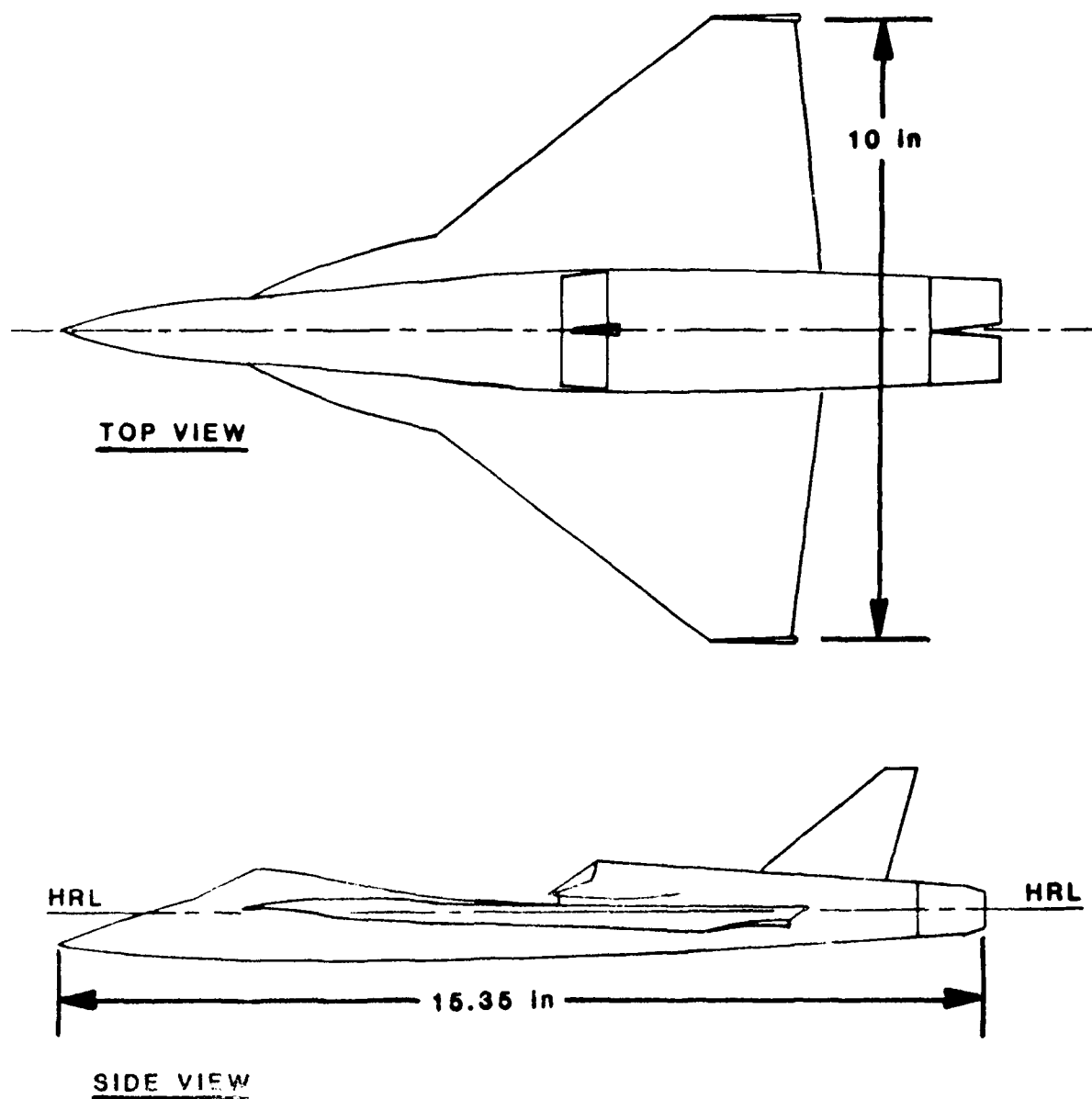
1/40th Scale Northrop VATOL Model

Figure 20. NORTHROP TOP-MOUNTED INLET VATOL CONCEPT

In a vertical flow, local total pressure should decrease through the wake because of viscous effects. This requires the coefficient $(_{TOTAL} = \frac{P_{oL} - P_o}{P_o - P_\infty})$ to be a negative value. The results of Jonas' pressure measurement comparison are shown in Table 1 below (Ref. 26).

	Seven-Hole Pressure Probe	Total Pressure Probe Aligned with Freestream	Aligned with Local Flow
Number of Available Total Pressure Readings			
Average Value	+0.197		
Standard Deviation	-0.008		
Maximum Value	--	-0.	+0.
Minimum Value	--	-0.007	
Number of Positive Values	--	18	

Jonas explains the following discussion based on the results of Table 1 data. As can be seen from the data, the total pressure probe measurements do not agree with seven-hole pressure probe measurements. For the total pressure probe aligned with the freestream flow, no measurements existed where P_{oL} was positive. However, these values may not be an accurate measure of local total pressure because flow angularity may have caused separation at the probe tip. For the total pressure probe aligned with the local flow, 26 percent of the measurements resulted in a local total pressure greater than that of the freestream value. These measurements, however, are lower than those obtained with

42

the seven-hole probe. One must realize that the total pressure probe was bent at an angle based on measurements made using the seven-hole pressure probe. Since the seven-hole measurements were made in a region of high shear flow, the local flow angularity reading may also be erroneous. Consequently, the flow around the tip of the total pressure probe supposedly aligned with the local flow might also be separated, again leading to false pressure readings. The average value for C_{TOTAL} of the bent total pressure probe, however, remains negative. This evidence seems to confirm our theoretical expectations of viscous effects.

Although the contradictive probe readings seem to indicate incorrect probe measurements in the high shear regime, the possibility of positive C_{TOTAL} regions may not be totally excluded. A vortex flow is very complex and not completely understood. Comparisons in a low shear flow environment (airfoil wake) of seven-hole probe measurements and hot-wire anemometer measurements are, however, very favorable and no discrepancies or positive C_{TOTAL} measurements exist (Ref. 26). This seems to indicate that the problem of positive C_{TOTAL}'s are only associated with high shear flows, and are ... ... due to the probe (manufacture, calibration, ...

... ... high shear flow environments.

... Construction

A pressure probe should be as small as possible to keep the flow ... ... disturbed; however, it is ... ... construction disadvantages. For example, smaller probes ... ... As size decreases,

tubes and other manufacturing imperfections cause greater in
construction errors, and the port tubes are more likely to ...

Although the five-hole probe may seem easier to construct than
the seven-hole, the exact opposite is true. The construction
of the seven-hole probe is greatly simplified since the port
tubes are arranged in the only geometric fitting possible.
Gallington and Hollerbaugh (Ref. 20) explain that the ...
that this geometric arrangement overcomes difficulties which
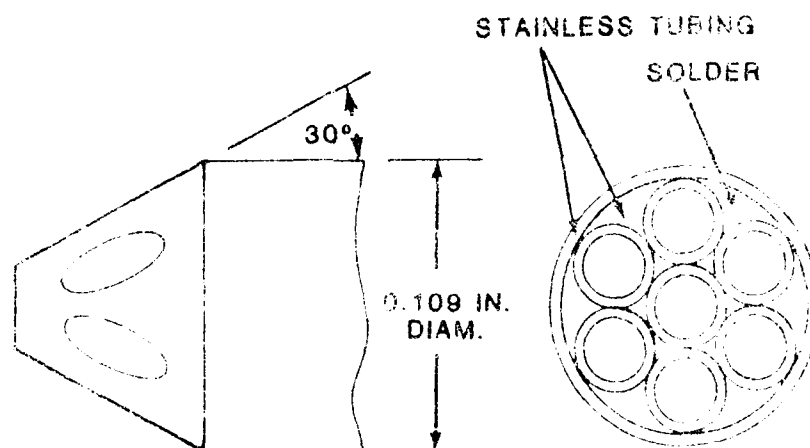exist in the five-hole probe.

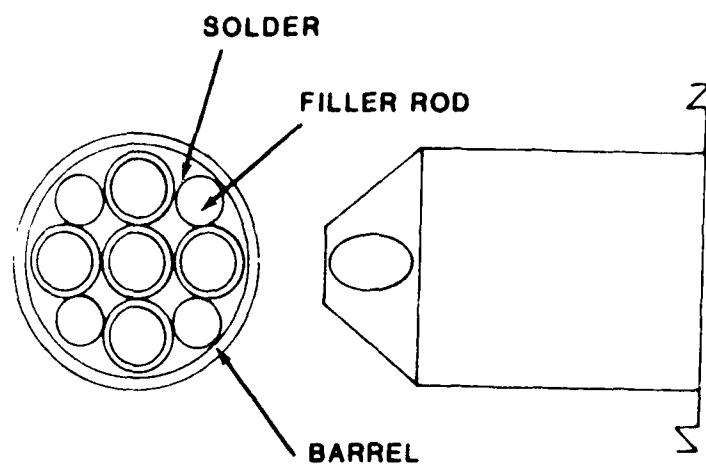Figure 21. SEVEN-HOLE PROBE CONSTRUCTION

Figure 22. CONVENIENT PROBE DESIGN

First, it is difficult to hold five-hole tubing parallel with the center tube and in perfect azimuthal position for soldering. Second, a high-powered magnifier is required to assure equal solder on the four side tubes. Finally, there is no guarantee that the four solder fillets shown below will be equal or even nearly equal.
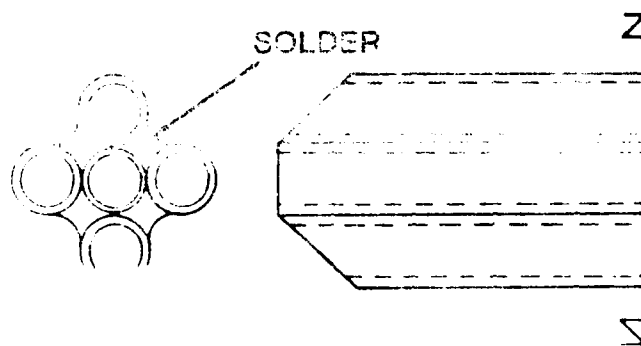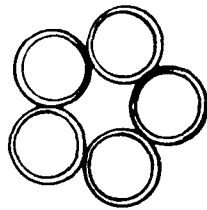

Figure 23. FIVE-HOLE PROBE ASSEMBLED FROM TUBES

As a quick note, a simpler geometric arrangement for five tubes is shown below. This order, however, lacks the required center tube.

Figure 24. FIVE TUBES IN
THE SMALLEST
CIRCUMSCRIBED
CIRCLE

Over the years, multi-hole probe construction has uncovered certain features that increase the accuracy of pressure measurement. Total pressure measurement can be largely desensitized to alpha and beta by flaring the stagnation port at an angle of 30 to 60 degrees. Yet, the probe's overall sensitivity to flow angularity can be increased by decreasing the tip half-angle (ϵ). The drawback to a small half-angle is that the flow will separate from the leeward surface when α_T exceeds ϵ (Ref. 1).

C. Measurement Error Sources

Once smaller probes are built, they are more sensitive to measurement errors caused by flow debris and damage. These two effects can be minimized prior to use by reverse airflow through clogged ports, by dust covers over port entrances, and by simple,

careful handling of smaller probes.

Huffman identifies three other error sources that adversely affect a probes measurement of pressure, orientation, and velocity (Ref 1). These sources include the time lag between sensed and actual pressures, the pressure transducer resolution and frequency response, and the resolution of the analog-to-digital conversion. The pressure transducer resolution and analog-to-digital resolution are both beyond the scope of this report; however, the other error sources are discussed in the following paragraphs (Ref. 1).

As flow field conditions change, the probe surface pressures change nearly instantaneously. These pressure changes are transmitted to the pressure transducers by a finite amount of air through a connection tube. Huffman discusses the fact that the pressure lag caused by this finite travel time is related to the speed of pressure propagation and the pressure drop due to the viscous effects of the tubing (Ref 1). Three physical characteristics directly affect this time lag:

1. Tubing diameter

2. Tubing length

3. Transducer cavity

As the tubing diameter decreases or as the tubing length increases the pressure lag increases. For a larger transducer cavity volume, it takes longer for the pressure pulse to propagate from the tubing exit.

Dunlapkohl and Buzzell (Ref 28) define frequency response as

> the inverse of the maximum dwell time necessary for the
> probe system to react to the maximum pressure difference
> expected where the pressure sensed by the pressure
> transducer reaches 99 percent of the actual (surface)
> pressure.

Although pressure time lag is the major factor in the probe's frequency response, it is not the sole contributor. The frequency response of the transducer, the computational time required to convert the measured pressure to the desired output, the pressure differential between the probe tip and the transducer face, and the fluid density all affect the probe's overall frequency response (Ref. 28).

Probe frequency response rates are generally of a few Hertz. Because modern transducers and microprocessors require only milliseconds to operate, their operation is essentially instantaneous, and little can be accomplished in these areas to decrease the overall frequency response. The final two factors are associated with the fluid dynamic properties of the flow. The difference between the fluid pressure at a port entrance and the pressure at the transducer face acts as a driving potential, and a greater differential increases the frequency response (Ref. 28). Since a higher density increases the collision rate between molecules, and therefore, increases the propagation rate of a pressure pulse, greater density is synonymous with greater frequency response. In considering the effect of density, one must remember the assumption of a constant static pressure across the face of the probe. Remembering $P = \rho RT$, one should realize that the density of the flow is dependent upon pressure.

Measurements of Unknown Flows

... with the seven-hole probe center on two

... the capabilites and limitations of the

... to map unknown flow fields. The following

... two objectives are accomplished in the

... flow.

... vortex flow, a finite wing section of a NACA

... placed in the two by three foot subsonic wind

... United States Air Force Academy (Figure 25). The

... with the wing at an angle of attack of 8 degrees and

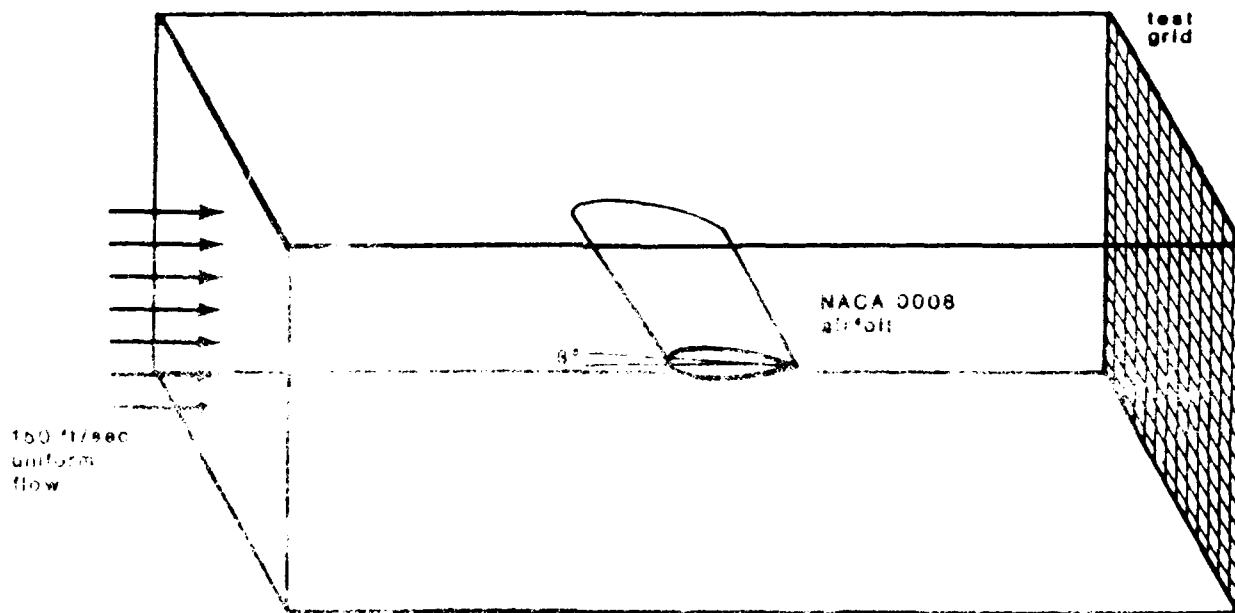... free flow velocity of 150 ft/sec.

Figure 25. WING VORTEX TEST

Computer graphing techniques were used to map out the flow
velocities and directions for all the points in a series of
parallel two-dimensional planes, all of which were perpendicular to
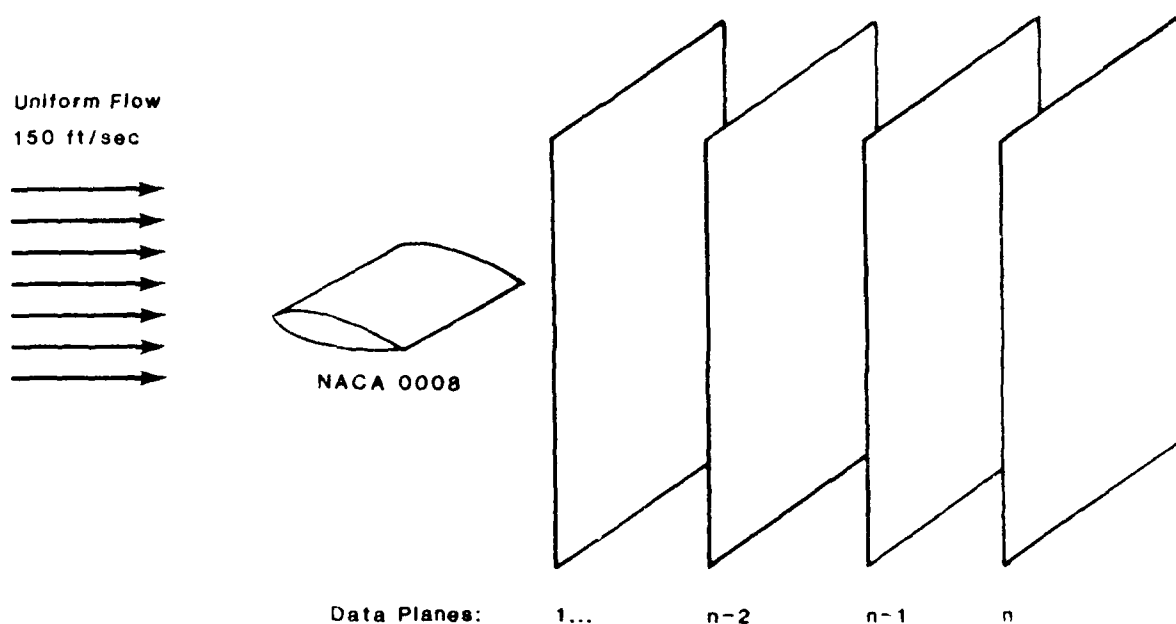the uniform flow.

**Uniform Flow
150 ft/sec**

NACA 0008

Data Planes: 1...   n-2   n-1   n

Figure 26. **WING VORTEX DATA PLANES**

The two-dimensional planes or test girds, started twelve inches aft of the wing's trailing edge and moved forward (toward the wing) by two inch increments for every data set. From these test runs, capabilities and limitations of the seven-hole probe under mild gradient conditions are examined and a wingtip vortex is mapped.

n. Crossflow Velocities

The first step in vortex analysis is to examine the crossflow velocities in each plane. Crossflow velocity plots, which are scaled by a factor of two are shown in Figures 27a to 27h (Ref. 29). With past errors in gradient regime, one would expect errors in seven-hole readings. Suspect data of this nature (Ref. 29) are identified by inconsistencies in the crossflow plots, such as an inordinately large or small arrow (Fig. 28) or an arrow in the wrong direction. However, the actual crossflow plots do not confirm these expectations. The velocities are well-behaved, and no inconsistancies are seen near the vortex core where high shear exists.
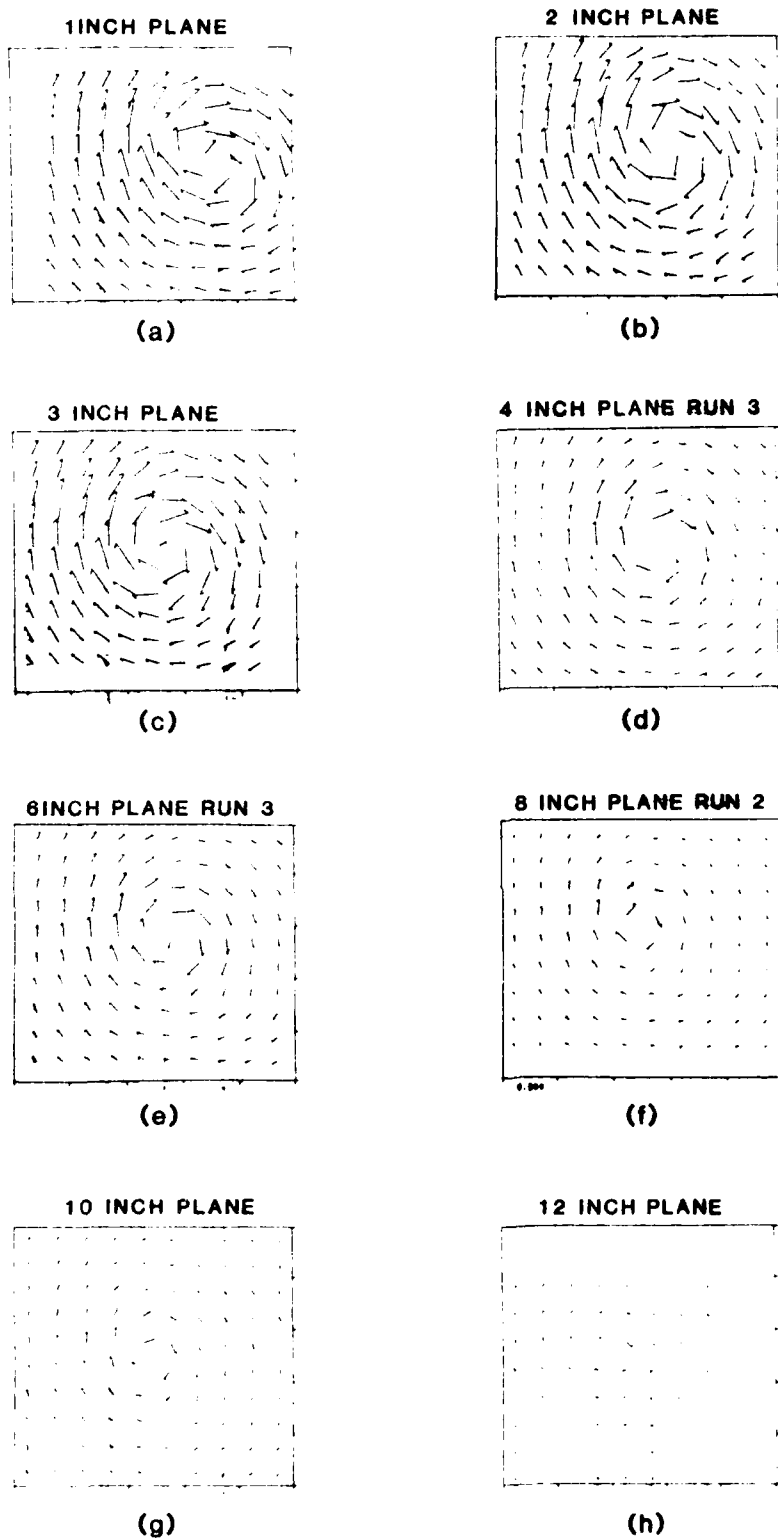
1INCH PLANE

(a)

2 INCH PLANE

(b)

3 INCH PLANE

(c)

4 INCH PLANE RUN 3

(d)

6INCH PLANE RUN 3

(e)

8 INCH PLANE RUN 2

(f)

10 INCH PLANE

(g)

12 INCH PLANE

(h)

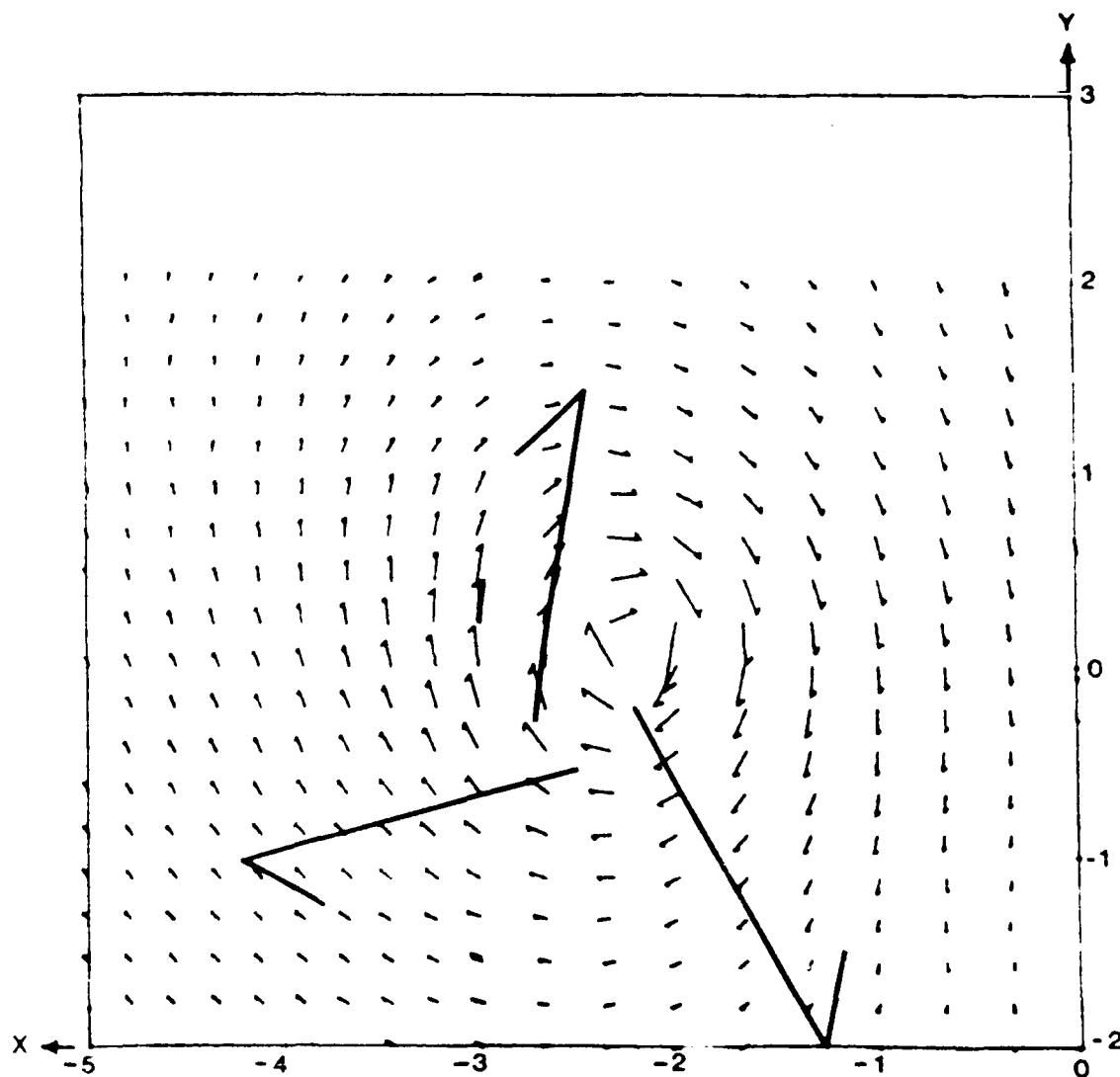Figure 27. CROSSFLOW VELOCITIES OF WING TIP VORE VORTEX

Figure 28. CROSSFLOW DATA ERRORS

...complete...velocity data may be shown on a velocity...centerline plot for ease of analysis (Figure 29).
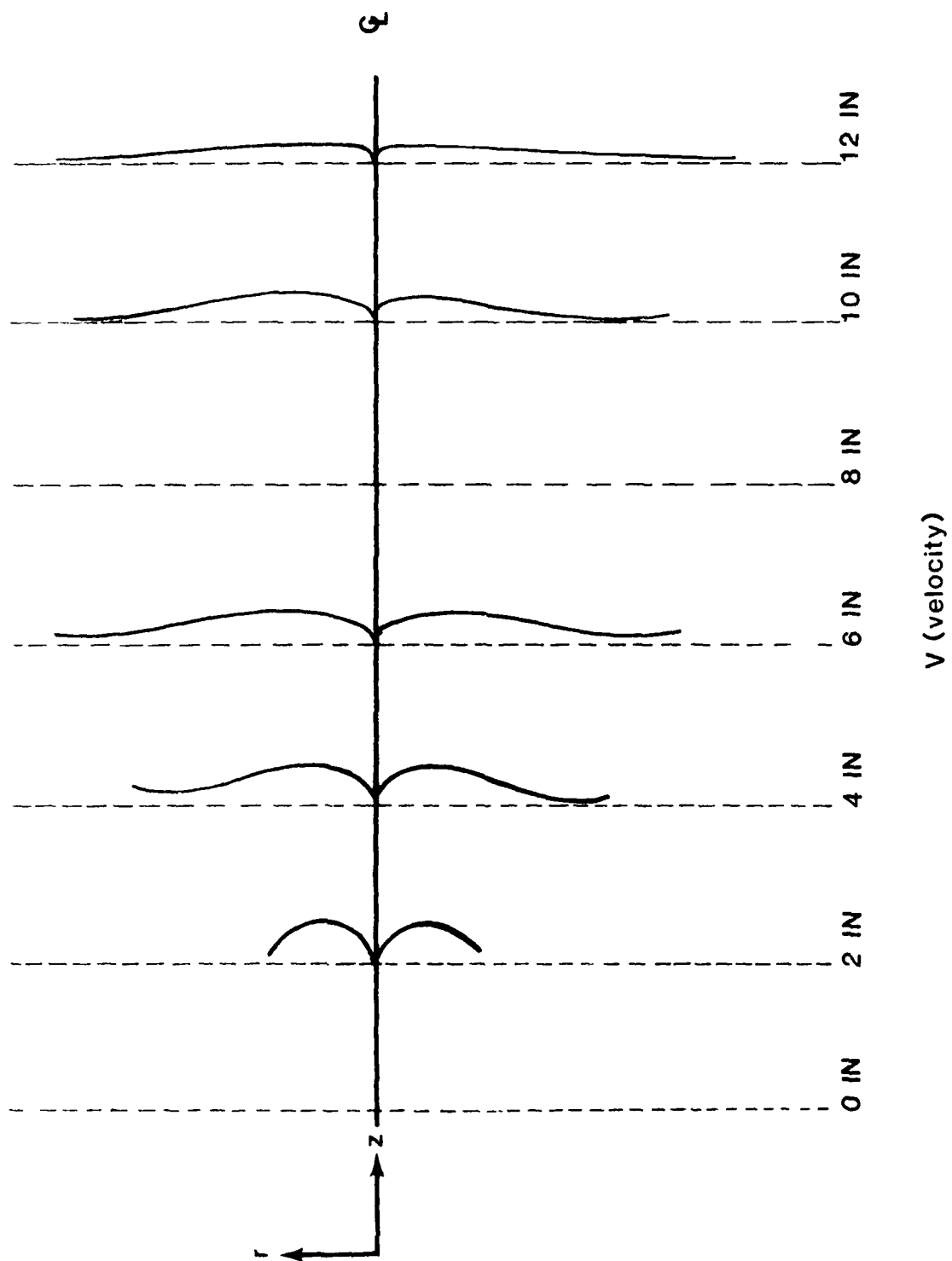
52

Figure 29. MAGNITUDE OF CROSSFLOW VELOCITY

52a

This new representation of the velocity data shows how the vortex expands and decays as it moves downstream. Represented by the velocity magnitude, the vortex strength decreases as the vortex expands. The vortex velocity gradient also decreases since the vortex is diffusing. Discontinuities do occur, however, at the eight-inch plane. As seen in Figure 29, the velocity magnitudes are smaller than those for the six-inch plane, but they are also smaller than those in the ten-inch plane. This data must be incorrect, for the vortex cannot be weaker at eight inches downstream than it is at ten inches. Because of the suspect data, the eight-inch plane is removed from future analysis.

In order to find a point at which the velocity gradient in the flow is great enough to induce noticeable error, additional measurements were taken at planes one-quarter and one-half inch behind the trailing edge. Again, the seven-hole probe exceeds expectations by revealing no such noticeable error. The crossflow plots for the two additional planes are shown in Figures 30a and 30b and are scaled by a factor of ten.
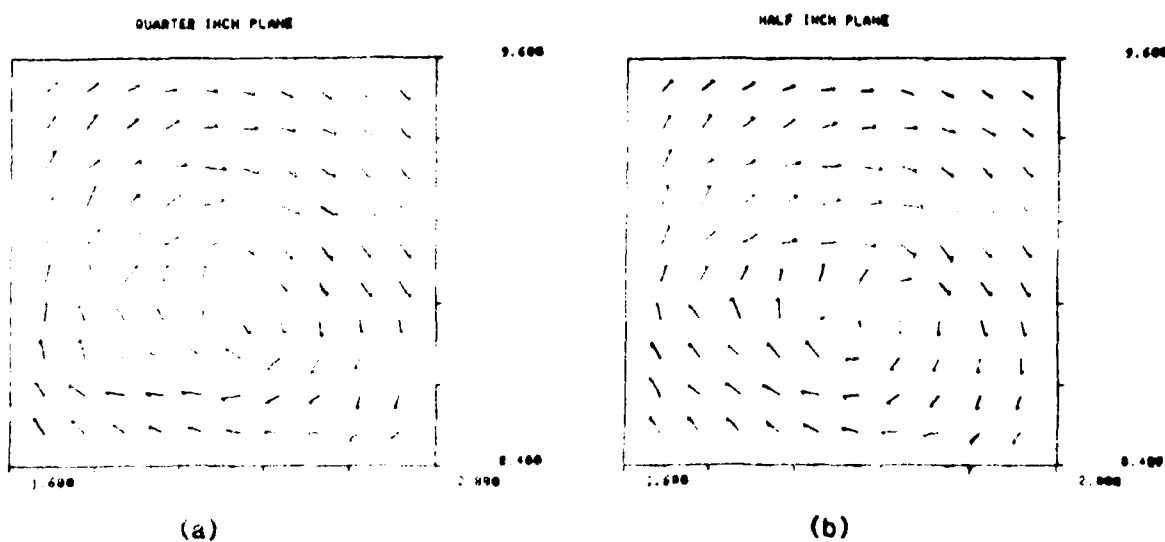

(a)   (b)

Figure 30. CROSSFLOW VELOCITY OF WING TIP VORTEX

C.   Definition of Flow Field Pressure Coefficients

Because pressure measurements are affected by slight shifts in wind tunnel velocity and temperature, pressure coefficients are used when the local and total tunnel pressures are compared and non-dimensionlaized by the tunnel dynamic pressure.   These three coefficients are defined below:

$$C_{STATIC} = \frac{P_{\infty L} - P_{\infty}}{P_0 - P_{\infty}}$$
$$C_{TOTAL} = \frac{P_{oL} - P_0}{P_0 - P_{\infty}}$$
$$C_{DYN} = C_{TOTAL} - C_{STATIC} = \frac{P_{oL} - P_{\infty L}}{P_0 - P_{\infty}} - 1$$

(39)

Probe measurement errors may be found by determining the correct values for these three pressure coefficients, either theoretically or experimentally with another device, and comparing these values with actual seven-hole probe data.   Vortex pressure coefficient trends may be found through analysis of a two-dimensional vortex.

D. C_{TOTAL}

For an ideal two-dimensional vortex, angular velocity increases inversely as the distance to the vortex center decreases (Figure 31).   Real vortices, however, are subject to viscous effects.   Outside of point A, the flow is essentially inviscid. Inside that point, viscous forces reduce angular velocity until it reaches zero at the vortex center.
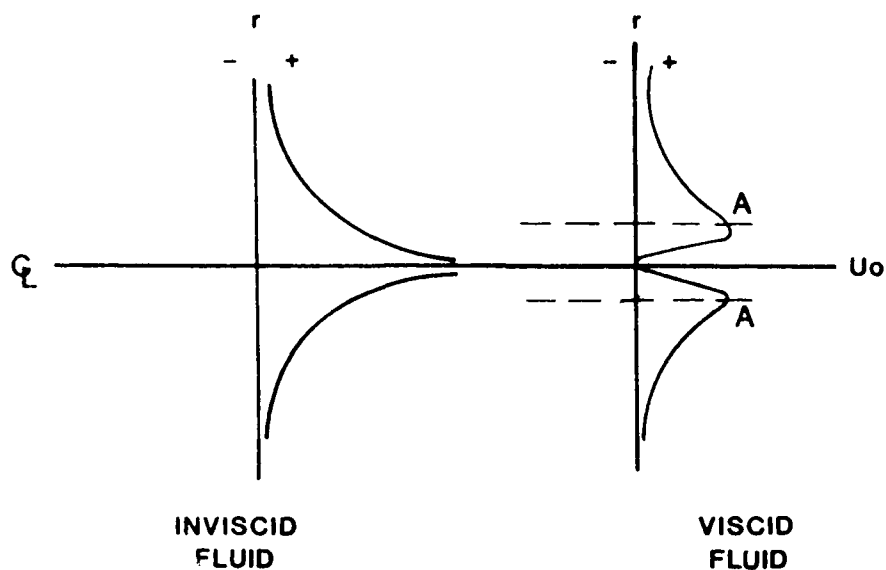
54

INVISCID FLUID   **VISCID FLUID**

Figure 31. ANGULAR VELOCITY OF VORTEX

These two flow regions directly affect C_{TOTAL} values. Because total pressure is constant in incompressible, inviscid flow, C_{TOTAL} is zero in the inviscid region. On the other hand, the viscous forces found within the vortex core decrease the flow's fluid-mechanical energy. P_o decreases causing C_{TOTAL} to become positive. Figure 31 diagrams C_{TOTAL}'s expected behavior.
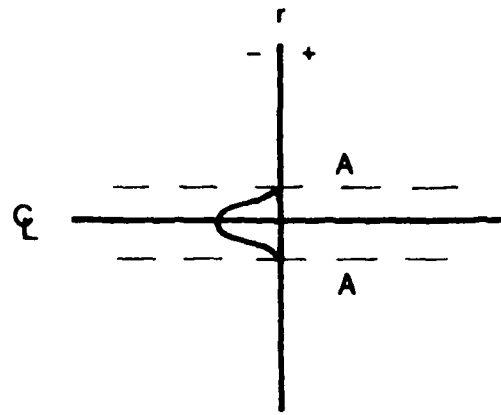
$$C_{TOTAL}$$

Figure 32. VORTEX C_{TOTAL}

The expected shape was derived by Jonas (Ref. 26) from theoretical considerations of a 2-D vortex decaying with time (Equation 40).

$$\frac{\partial P_{CL}}{\partial r} = \frac{\rho}{r} \left(\frac{\Gamma_1}{2\pi}\right)^2 \frac{1}{2\nu t} e^{-r^2/4\nu t} (1-e^{-r^2/4\nu t}) \tag{40}$$

As discussed, the bucket-shape phenomenon is present in the experimental vortex data shown in Figure 33.
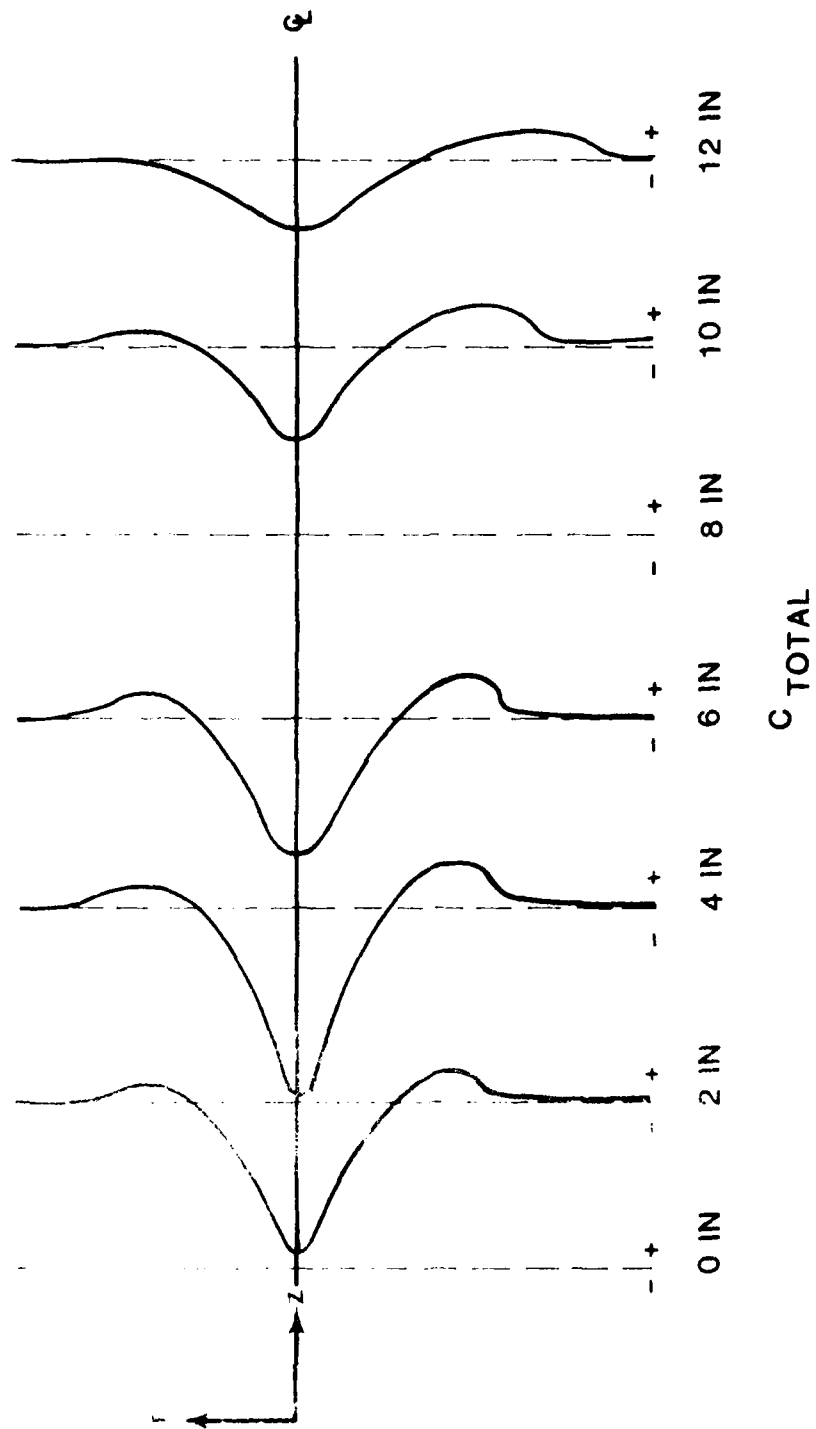
Figure 33. C_{TOTAL} OF WING VORTEX

As the flow progresses downstream, lower velocity gradients produce smaller viscous forces, smaller deficits of fluid-mechanical energy, and small bucket-shaped area plots. The two areas of positive C_{TOTAL} in each of the centerline plots is unexpected. The fact that the magnitude of the positive C_{TOTAL} values is always greater on the outboard side of the wing than on the inboard side is inexplicable. The sets of contour plots and axonometric plots (Appendix A) show that C_{TOTAL} is positive only on the two sides of the vortex parallel to the wing. The vortex data behaved normally above and below the wing. In duplicating Jonas's previous positive C_{TOTAL} results the vortex data seem to indicate a limitation in the seven-hole probe's measurement capabilities. It is still possible, however, that the positive C_{TOTAL} values may be the result of a transfer mechanism that is not yet understood.

E. C_{STATIC}

Like C_{TOTAL}, the presence or absence of viscosity affects the values of C_{STATIC}. At freestream conditions, C_{STATIC} equals zero. Progressing inward from the freestream conditions to point A, the angular velocity increases, static pressure drops, and C_{STATIC} decreases from zero to a negative value. To determine what happens in the viscous region, the following mathematical analysis is required.

$$\frac{dp}{dr} = \frac{\rho u_\theta^2}{r}$$

For a free vortex $u = \frac{c}{r}$ so, $\frac{dp}{dr} = \frac{\rho c^2}{r^3}$

For solid body rotation $u_\theta = \omega r$ so, $\frac{dp}{dr} = \rho \omega^2 r$

57

Integrating for p results in the following:

$$P = C_1 - \frac{\mu C^2}{2r^2}$$ (41a)

$$P = C_2 + \frac{\rho w^2 r^2}{2}$$ (41b)

Equations 41a and 41b when superimposed reveal a bucket-shape like that of C_{TOTAL}. The entire C_{STATIC} curve is shown in Figure 34.
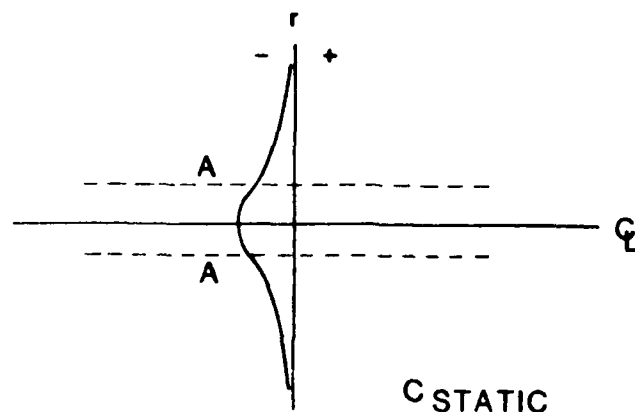

Figure 34. VORTEX C$_{STATIC}$

E. C$_{DYNAMIC}$

$C_{DYNAMIC}$ is simply the subtraction of C_{STATIC} from C_{TOTAL} as shown in equation 36. Again, at the freestream, $C_{DYNAMIC}$ is ideally zero. $C_{DYNAMIC}$ equals the absolute value of C_{STATIC} from the freestream conditions inward to point A since C_{TOTAL} is zero. At the center of the vortex, local velocity and therefore local dynamic pressure are zero causing $C_{DYNAMIC}$ to equal -1. From point A to the center, $C_{DYNAMIC}$ changes as in Figure 35.
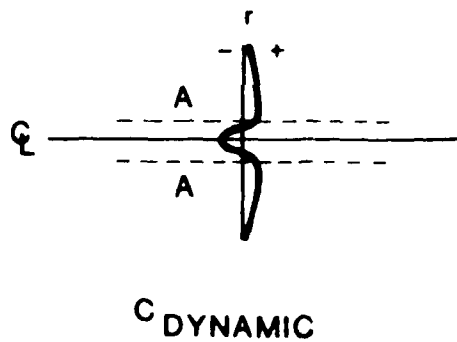
Insert Figure 35

$$C_{DYNAMIC}$$

Figure 35. VORTEX C$_{DYNAMIC}$

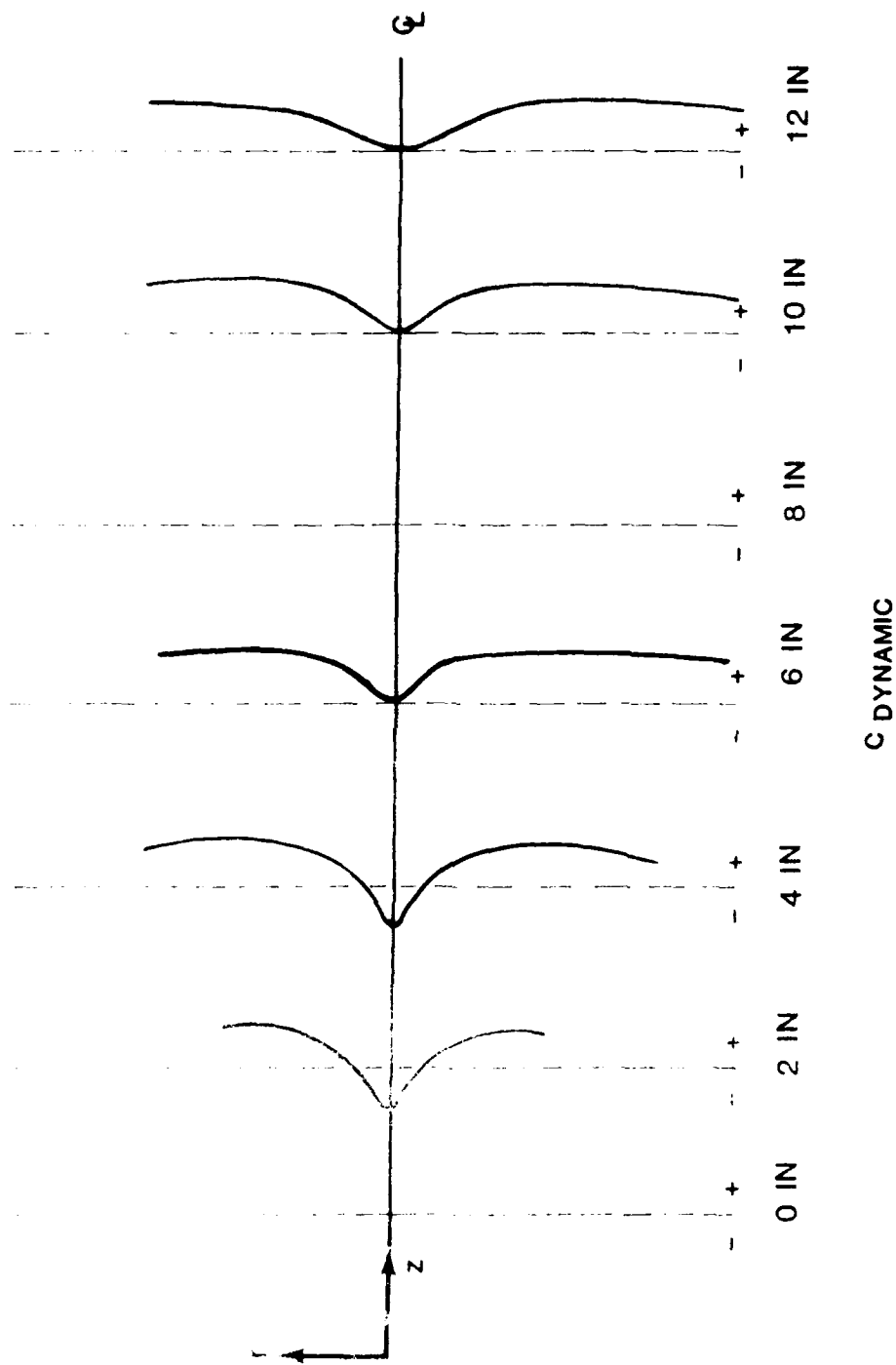Experimental data supports the theoretical analysis of C_{DYN}.

Figure 36. $C_{DYNAMIC}$ OF WING VORTEX

This seems somewhat surprising in lieu of the questionable positive C_{TOTAL} values. The important factor missing from the coefficient plots are the relative magnitudes. Because C_{TOTAL} values are very close to zero, the contribution of C_{TOTAL} is not very significant in the calculation of $C_{DYNAMIC}$.

3. Research Applications

Today's flow mapping efforts are much more complex than the vortex example. Besides Jonas' VATOL flow field measurements, seven-hole probe work at the Air Force Academy has examined canard wakes, lifting surface wakes of canard/swept wing aircraft, and flow field characteristics of square cross-sectional missile bodies. Probe calibration and measurement of unknown flowfields have also been conducted at the NASA Ames Research Center in the 2x2 foot and 14 foot transonic wind tunnels (Ref. 30). Measurements of wing and canard jet-flap effects as well as the effects of prop fan installations have been made with multiple and single proble installations. Yet, these more complex research efforts are founded on the basic analysis and data presentation explained in the vortex example.

Griffin (Ref. 31) used cross velocity and pressure contours in his study of canard/forward swept wing aircraft. Figures 37 and show the two types of data plots in the same spatial relationship that their data points have to the model.

Figure 37. TYPICAL VELOCITY DATA
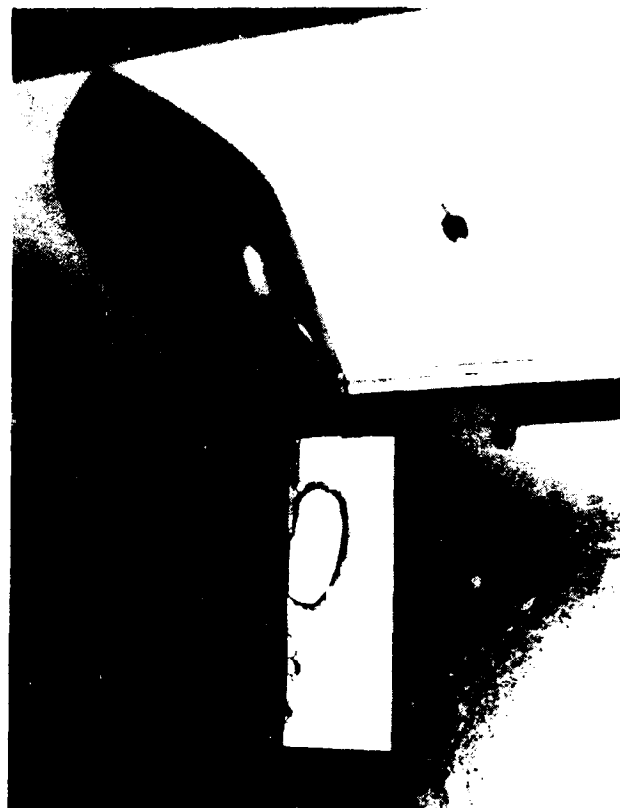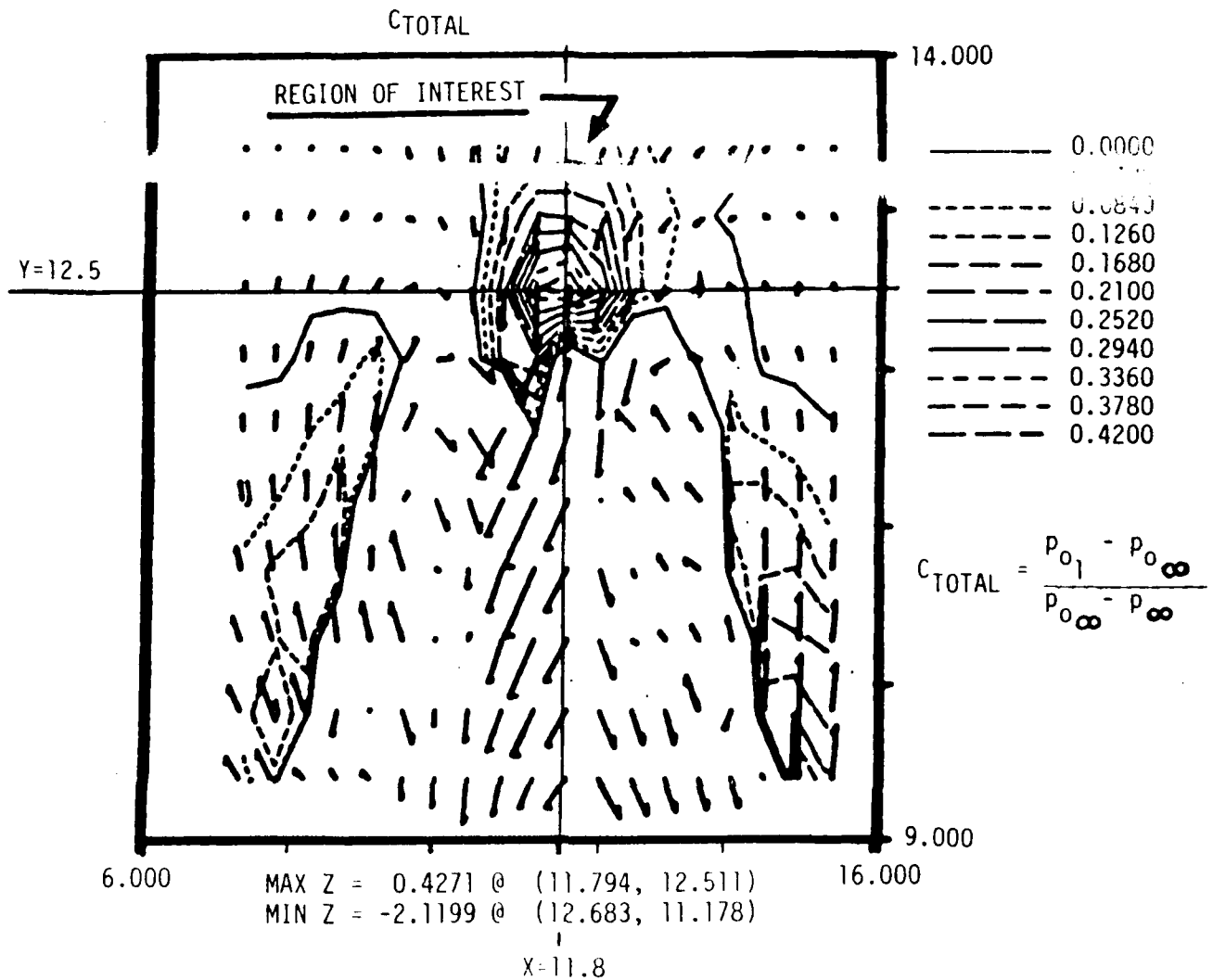PLANE LOCATION
RELATIVE TO MODEL

Figure 38. TYPICAL PRESSURE DATA
PLANE LOCATION
RELATIVE TO MODEL

Jonas (Ref 26) superimposed these two types of plots in his

investigation of C_{TOTAL} (see Figure 39).

NASA MODEL, STRUT MOUNT, ZMP75   20:31   14-SEP-82

C_{TOTAL}

REGION OF INTEREST

Y=12.5

14.000

0.0000
0.0840
0.1260
0.1680
0.2100
0.2520
0.2940
0.3360
0.3780
0.4200

$$C_{TOTAL} = \frac{P_{0_1} - P_{0_\infty}}{P_{0_\infty} - P_\infty}$$

9.000

6.000

MAX Z = 0.4271 @ (11.794, 12.511)
MIN Z = -2.1199 @ (12.683, 11.178)

16.000

X=11.8

Figure 39. REGIONS OF POSITIVE C $_{TOTAL}$, DATA PLANE ZMP75

Jonas also used a series of axonometric projections to analyze the

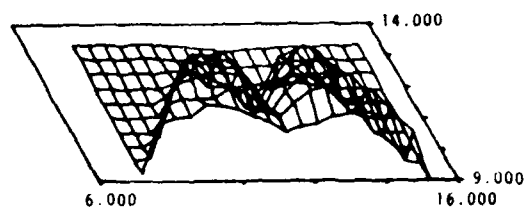growth (diffusion) and decay (dissipation) of vortices.

Evidence of mixing is found in the relative flattening of the

C_{TOTAL} values (negative C_{TOTAL} being up or out of the plane of
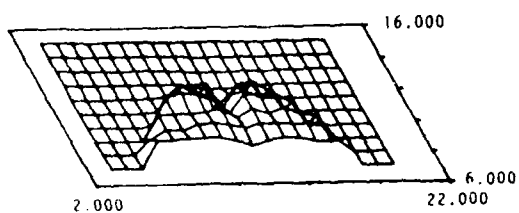
projection).

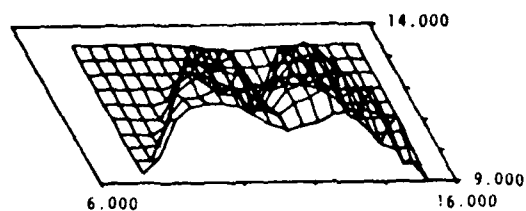NASA MODEL, STRUT MOUNT, ZP6   15:27   16-SEP-82
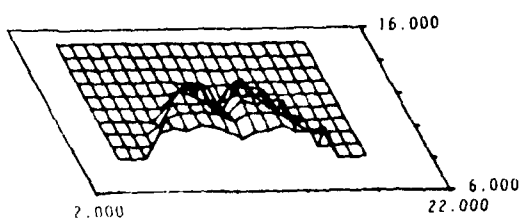CTOTAL
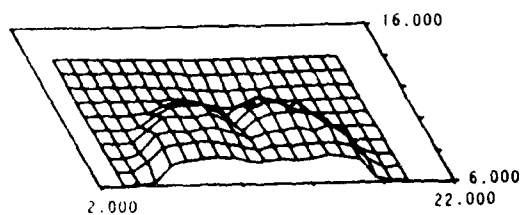
NASA MODEL, STRUT MOUNT, ZO
CTOTAL

NASA MODEL, STRUT MOUNT, ZP2   14:46   16-SEP-82
CTOTAL

NASA MODEL, STRUT MOUNT, ZMP25
CTOTAL

NASA MODEL, STRUT MOUNT, ZP1   12:15   16-SEP-82
CTOTAL

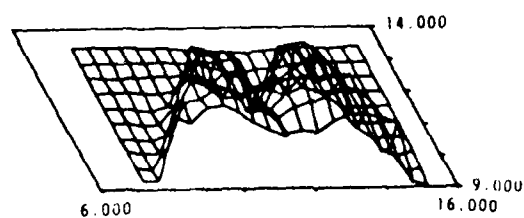NASA MODEL, STRUT MOUNT, ZMP5   19:53   14-SEP-82
CTOTAL

Figure40. AXONNMETRIC PROJECTIONS, C $_{TOTAL}$, DATA PLANES ZP6 TO ZMP5

62a

Gerner and Durston at NASA Ames took Jonas' data and produced
a series of 12 color contour photographs that span the development
through decay of the VATOL vortices. The study was limited to the
examination of local total pressure or C_{TOTAL}. The color contours
allow more detail in data representations by making pressure
differences easier to see. Regions of positive C_{TOTAL} are clearly
distinguished from other points in the flow field. As seen in the
other data schemes, the color contours reveal that the VATOL is in
a slight sideslip. This causes the right vortex to burst prior to
the left vortex.

VII. Conclusions

As shown, the seven-hole pressure probe remains a valuable
measurement tool for the documentation of unknown flowfields. The
device has a greater measurement range and flexibility than other
similar obtrusive flow measuring devices. The seven-hole probes
themselves are easily constructed and calibrated for use in
subsonic compressible flows. Measurements in adverse shear flows
can be corrected to give actual flow conditions based on the
methodology developed in this paper. Finally, as shown in the
application section, the probe is not only a valuable research
device but educational as well in demonstrating fundamental flow
properties.

VIII. Acknowledgement

The authors would like to acknowledge Lt. Col. Roger
Gallington, who developed the methodology for the seven-hole
pressure probe. The authors would also like to thank Mr. Don
Durston of the NASA Ames Research Center and the faculty and cadets
of the USAF Academy who aided in the completion of this effort.

Symbols

A_i the ith value of a particular data point either known or determined from calibration equations

C_{DYN} local dynamic pressure coefficient

C_{APM} coefficient representative of compressibility effects

C_0 apparent total pressure coefficient

C_p coefficient of pressure

C_q apparent dynamic pressure coefficient

C_{STATIC} local static pressure coefficient

C_{TOTAL} local total pressure coefficient

C_α angle of attack pressure coefficient

C_β angle of sideslop pressure coefficient

C_ϕ roll angle pressure coefficient

C_θ pitch angle pressure coefficient

f body geometry function

K_i calibration coefficients

l length

M Mach number

P pressure

q dynamic pressure

(r, θ, z) cylindrical coordinates

R radius

s distance between centers of opposing holes

u local velocity, perturbation velocity component

V velocity

(x, y, z) Cartesian coordinates

α angle of attack

β angle of sideslip

δ	$\sqrt{1-M_\infty^2}$
ϵ	probe tip half angle
ζ	ratio of specific heats
ϕ	roll angle
ρ	density
υ	pitch angle

subscripts

C	uniform incompressible flow
(i,j)	local property or condition
o	total or stagnation condition
	freestream conditions

References

1. Huffman, G.J.D., Theory, Performance and Design of Flow Direction and Mach Number Probes, AFATL TR-81-44, Air Force Armament Laboratory, Eglin AFB, Florida, April 1981.

2. Gerner, A.A. and C.L. Mauer, "Calibration of Seven-Hole Probes Suitable for High Angles in Subsonic Compressible Flows," Aeronautics Diges, USAFA-TR-81-4, USAF Academy, Co., May 1981.

3. Schultz, W.M. et.al., "Several Combination Probes for Surveying Static and Total Pressure and Flow Direction, NACA TN 2830, 1952.

4. Kettle, D.J., "Design and Calibration at Low Speeds of a Static Tube and Pitot-Static Tube with Semi-Ellipsoidal Nose Shapes," J. Ray. Aero. Soc., Vol. 58, p. 835, 1954.

5. Smetena, F.O. and J.W.M. Stuart, A Study of Angle-of-Attacks Angle-of-Sideslop Pitot-Static-Probes, WADC TR 5723A, AD 118209, 1957.

6. Bryer, O.W. et.al., "Pressure Probes Selected for

Three-Dimensional Flow Measurement," Rep.Mem. Aero Res. Coun. London, No. 3037, 1958.

7. Morrison, D.F. et.al., "Hole Size Effect on Hemisphere Pressure Distributions." J.Roy. Aer. Soc., Vol. 71, 1967.

8. Wright, M.A., "The Evaluation of a Simplified Form of Presentation for Spherical and Hemispherical Pitometer Calibration Data," J. Sci. Instr. (J. Phys. E). Vol. 3, p. 456, 1970.

9. Schaub, V.W. et.al., An Investigation of the Three-Dimensional Flow Characteristics of a Non-Nulling Five-Tube Probe, Nat. Res. Council of Canada, Aero Rpt. LR-393, NRC No. 7964, 1964.

10. Dudzinski, J.T. and L.N. Krause, Flow Direction Measurement with Fixed-Position Probes, NASA TMX-1904, 1969.

11. Beecham, L.J. and S.J. Collins, Static and Dynamic Response of a Design of a Differential Pressure Yawmeter at Supersonic Speeds, Roy. Aer. Est. Report No. GW 19, 1954.

12. Hutton, P.G., Static Response of a Hemispherical-Headed Yawmeter at High Subsonic and Transonic Speeds, Roy. Aero. Est. Tech. Note N. Aero 7525, CP No. 401, 1957.

13. Nowack, C.F.R., "Improved Calibration Method for a Five-Hole Spherical Pitot Probe," J. Sci. Instr. (J. Phys. E.), Vol. 3, p. , 1970.

14. Rees, R., et.al., "Nine Probes for the Measurement of the Complete Velocity Vector in Subsonic Flow," Aero. J., Vol. 72, p. , 1968.

15. Spaid, F.W. et.al., "Minature Probe for Transonic Flow Direction Measurement," AIAA J., Vol. 13, p. 253, 1975.

16. Glawe, G.E., et.al., A Small Combination Sensing Probe for Measurement of Temperature, Pressure and Flow Direction; NASA TN

D-4816, 1968.

17. Treaster, A.L. and A.M. Yocum, The Calibration and Application of Five-Hole Probes," Penn. State Univ. Applied Research Laboratory Report TM 78-W, 1978.

18. Bryer, D.W. and D. W. Pankhurst, Pressure Probe Methods for Determining Wind Speed and Flow Direction, Published by Her Majesty's Stationery Office, London, England, 1971.

19. Wuest, W., "Measurement of Flow Speed and Flow Direction by Aerodynamic Probes and Vanes," Paper Presented at the 30th Flight Mechanics Panel Meeting in Montreal, Canada, 1967.

20. Huffman, G. David, "Flow Field Characteristics of Flw Direction and Mach Number Probes Using Slender Body Theory," Aeronautics Digest, USAFA-TR-79 1, USAF Academy, CO, Feb. 1979.

21. Hess, J.L. and A.M.O. Smith, "Calculation of Potential Flwo about Arbitrary Bodies," Progress in Aeronautical Sciences, Vol. 8, Pergammon Press, p.81, 1966.

22. Smith, A.M.O. and A.B. Bauer, "Static-Pressure Probes that are Theoretically Insensitive to Pitch, Yaw and Mach Number," J.Fl. Mech., Vol.44 p. 513, 1970.

23. Liepmann, H.W. and A. Roshko, Elements of Gas Dynamics, John Wiley and Sons, New York, 1958.

24. Gallington R.W. "Measurement of Very Large Flow Angles with Non-Nulling Seven-Hole Probes," Aeronautics Digest, USAFA-TR-80-17, USAF Academy, Co., October 1980.

25. Reed,L.S. and G.H. Johnson, "Seven-Hole Probe in Shear Flow," AIAA Paper 85-0076 (to be published).
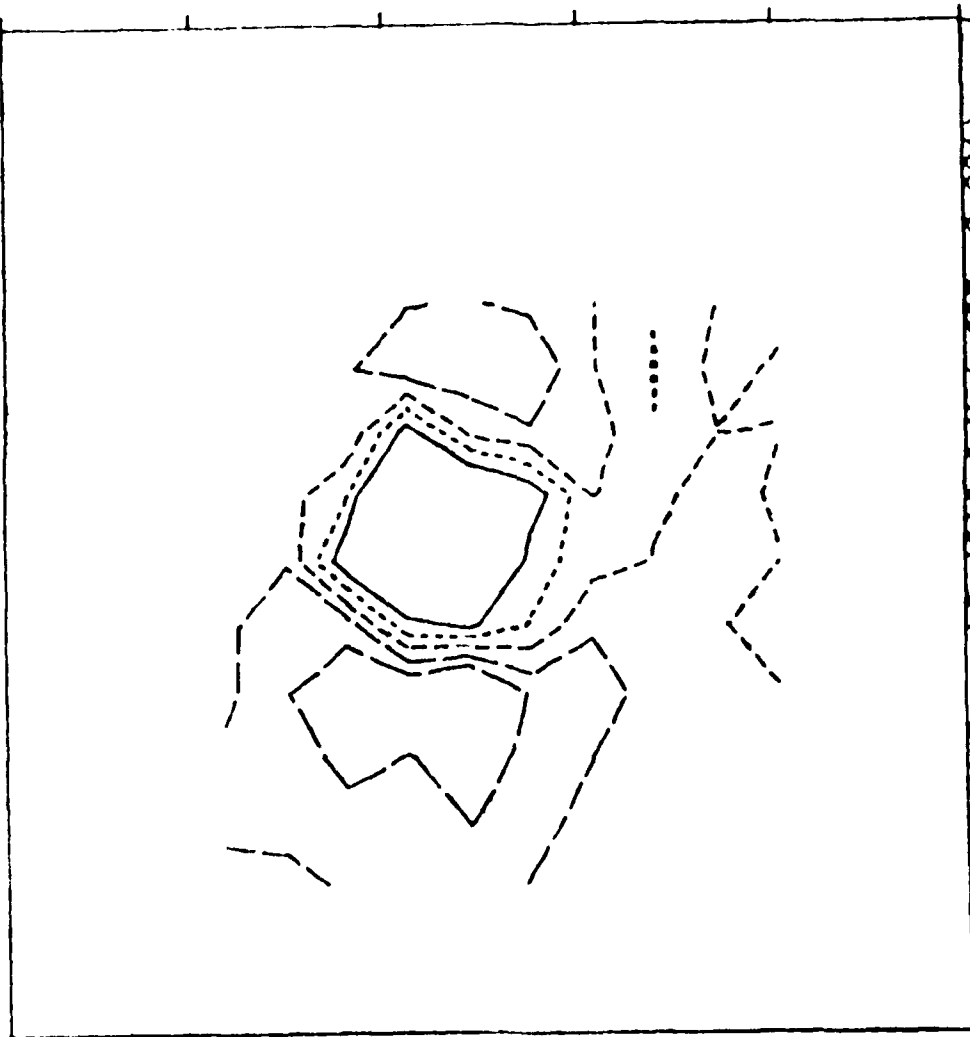
APPENDIX A

Wing Tip Vortex C_{TOTAL} Plots

2 INCH PLANE

CTOTAL

10.500

-0.2000
-0.1000
0.0000
0.1000
0.2000

0.500

7.000

4.000

MAX Z = -0.4910 @ (2.363; 9.803)
MIN Z = -0.7362 @ (2.592; 8.823)

Figure A-1

A-1

3 INCH PLANE

CTOTAL

10.500

    ───────   -0.2000
    ···········   -0.1000
    ─ ─ ─   0.0000
    ─ ─ ─   0.1000
    ─── ───   0.2000

MAX Z = -0.43000 @ (2.819, 0.0001)
MIN Z = -0.57000 @ (2.819, 0.0001)
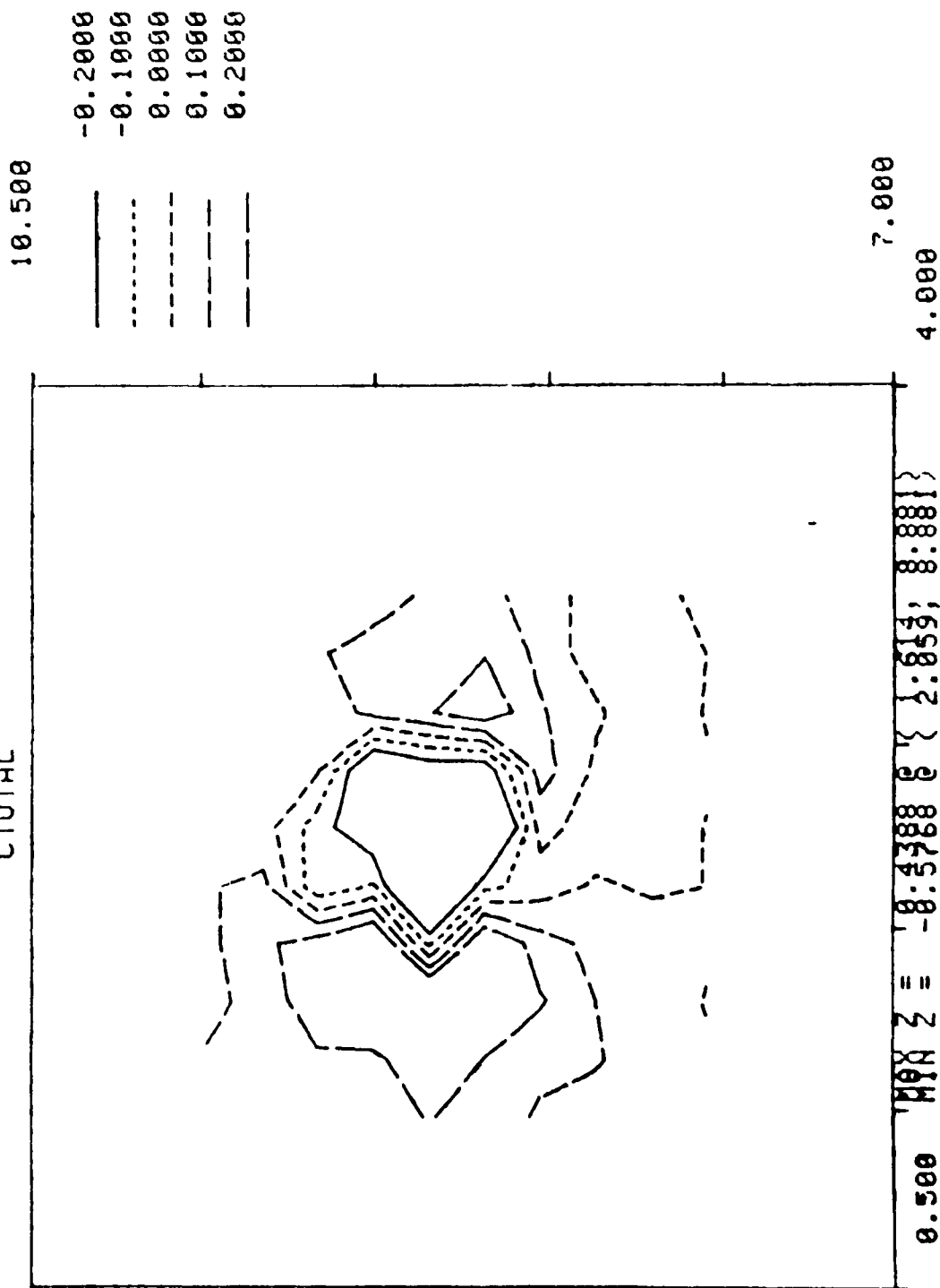
0.500

4.000

7.000

Figure A-2

4 INCH PLANE

CTOTAL

10.500

-0.2000
-0.1000
0.0000
0.1000
0.2000
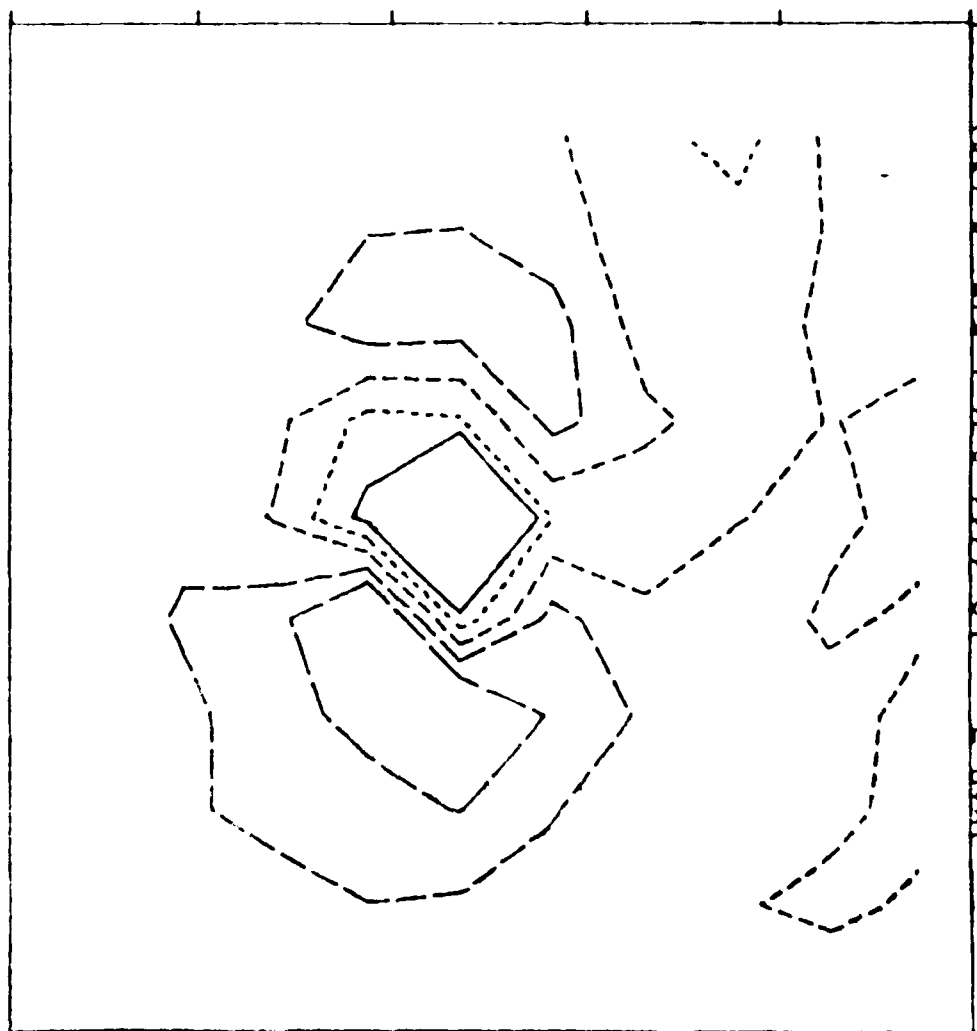
7.000
4.000

0.500   MAX Z = -0.0505 @ (2.277, 0.857)
        MIN Z = -0.0505 @ (2.277, 0.857)

Figure A-3

6 INCH PLANE

CTOTAL

-0.2000
-0.1000
0.0000
0.1000
0.2000

10.500

MAX Z = -0.4189 @ (2.790, 8.947)
MIN Z = -0.6627 @ (2.457, 8.947)

0.500

4.000

7.000

Figure A-4

1 INCH PLANE

CTOTAL 0.500

7.000
4.000

0.500

Figure A-5

2 INCH PLANE

CTOTAL 0.500

7.000

4.000

0.500

Figure A-6

A-6

3 INCH PLANE

7.000
4.000

CTOTAL 8.500

0.500

Figure A-7

4 INCH PLANE

CTOTAL 0.500

7.000
4.000

0.500

Figure A-8

A-8

END

FILMED

3-85

DTIC